Hemorrhage-activated NRF2 in tumor-associated macrophages drives cancer growth, invasion, and immunotherapy resistance

Schaer, Dominik J ; Schulthess-Lutz, Nadja ; Baselgia, Livio ; Hansen, Kerstin ; Buzzi, Raphael M ; Humar, Rok ; Dürst, Elena ; Vallelian, Florence

DOI: https://doi.org/10.1172/jci174528

Hemorrhage-activated NRF2 in tumor-associated macrophages drives cancer growth, invasion, and immunotherapy resistance

Dominik J. Schaer[1], Nadja Schulthess-Lutz[1], Livio Baselgia[1], Kerstin Hansen[1], Raphael M. Buzzi[1], Rok Humar[1], Elena Dürst[1], Florence Vallelian*[1]

[1] Department of General Internal Medicine, University Hospital and University of Zurich, Zurich, Switzerland

*Correspondence:
Florence Vallelian MD
Department of Internal Medicine
University Hospital, Ramistrasse 100
CH-8091 Zurich, Switzerland
florence.vallelian@usz.ch

ABSTRACT

Microscopic hemorrhage is a common aspect of cancers, yet its potential role as an independent factor influencing both cancer progression and therapeutic response is largely ignored. Recognizing the essential function of macrophages in red blood cell disposal, we explored a pathway that connects intratumoral hemorrhage with the formation of cancer-promoting tumor-associated macrophages (TAMs). Using spatial transcriptomics, we found that NRF2-activated myeloid cells possessing characteristics of procancerous TAMs tend to cluster in peri-necrotic hemorrhagic tumor regions. These cells resembled anti-inflammatory erythrophagocytic macrophages. We identified heme, a red blood cell metabolite, as a pivotal microenvironmental factor steering macrophages toward protumorigenic activities. Single-cell RNA-seq and functional assays of TAMs in 3D cell culture spheroids revealed how elevated intracellular heme signals via the transcription factor NRF2 to induce cancer-promoting TAMs. These TAMs stabilized epithelial-mesenchymal transition, enhancing cancer invasiveness and metastatic potential. Additionally, NRF2-activated macrophages exhibited resistance to reprogramming by IFNγ and anti-CD40 antibodies, reducing their tumoricidal capacity. Furthermore, MC38 colon adenocarcinoma-bearing mice with NRF2 constitutively activated in leukocytes were resistant to anti-CD40 immunotherapy. Overall, our findings emphasize hemorrhage-activated NRF2 in TAMs as a driver of cancer progression, suggesting that targeting this pathway could offer new strategies to enhance cancer immunity and overcome therapy resistance.

INTRODUCTION

Hemorrhage is omnipresent in solid cancers, occurring at macroscopic and microscopic levels due to invasive tumor growth, pathological vascularization, and therapy-induced or spontaneous necrosis. While traditionally perceived as a disease complication with occasional catastrophic clinical outcomes, the role of hemorrhage as a biological modifier influencing cancer progression and therapeutic responses remains unexplored, creating a unique research gap.

Macrophages, the primary immune cells patrolling the microenvironment of solid cancers, provide an intriguing link between tumor hemorrhage and cancer biology. With their dynamic phenotype and functional versatility, macrophages can respond to diverse spatiotemporal signals to either aid in disease control or contribute to cancer progression (1–4). Tumor-associated macrophages (TAMs) can adopt anti-tumoral functions when adequately activated by tumor-specific T-cells through interferon-γ (IFNγ) or CD40 signaling (5, 6). Conversely, anti-inflammatory cytokines and metabolic stressors, such as fluctuations in pH, electrolyte, or oxygen concentrations, can promote the emergence of procancerous TAMs (7–14). These procancerous TAMs have impaired tumoricidal functions, promote angiogenesis, enable epithelial-mesenchymal transition (EMT), and suppress T-cell functions (15–17). The discovery of cellular markers for procancerous TAMs such as SPP1 and CD163 (18–21) in humans and Arg1 (22) in mice has led to extensive research across many cancer types, confirming their association with poor disease outcomes (19, 21–23). As a result, repolarizing procancerous TAMs into cancer-fighting macrophages, for example, by agonistic anti-CD40 antibodies, presents a promising therapeutic avenue (24, 25).

In healthy and cancerous tissues, macrophages are pivotal in resolving hematomas, ensuring homeostasis, and fostering a microenvironment that promotes tissue repair (26). Macrophages possess unique capabilities to engulf damaged red blood cells (RBCs) and detoxify heme and iron by upregulating heme-oxygenase (HMOX1) and antioxidant metabolic pathways regulated by the transcription factor NFE2L2 (NRF2) (27). This macrophage response is considered a "cold" inflammation because it does not activate an immune response against self-antigens released en masse by damaged cells. However, this response may prove

counterproductive in a hemorrhagic tumor by fueling cancer growth in an immunologically cold tumor microenvironment (27, 28).

Our previous work revealed that heme, a metabolite derived from RBCs, activates NRF2 in macrophages, inducing a profound metabolic switch. The NRF2-polarized macrophages undergo reprogramming into erythrophagocytes with a reparative phenotype, compromised immune functions, and remarkable resistance to pro-inflammatory stimuli (27, 29). Interestingly, these NRF2-polarized erythrophagocytes share phenotypic similarities with procancerous TAMs, such as high HMOX1 and scavenger receptor MARCO expression, while MHC class II is profoundly suppressed. This observation suggests that hemorrhage-derived heme could be an overlooked factor in the cancer microenvironment, promoting the emergence of procancerous TAMs.

Here, we define a trajectory connecting intratumoral hemorrhage to the formation of cancer-promoting TAMs. By analyzing the transcriptomes of human cancers, peri-necrotic cancer microenvironments, and artificial hematomas, we discovered substantial similarities between heme-polarized reparative macrophages and cancer-promoting TAMs. Using innovative models to assess TAM functions in 3D cell culture and mice, we demonstrated that upstream heme signaling through NRF2 reprograms macrophages to fuel cancer growth, invasion, metastasis, and resistance to immunotherapy. Targeting and disrupting heme-NRF2 signaling in macrophages may enhance antitumor immune responses and amplify the effectiveness of existing immunotherapies.

RESULTS

Tumor hemorrhage connects with procancerous TAM identities

In the hemorrhagic tissue milieu, macrophages engulf RBCs, leading to pronounced induction of HMOX1 expression (30, 31). Building on this understanding, we postulated that HMOX1 expression within a comprehensive tumor gene expression dataset could serve as a marker for investigating the influence of microhemorrhage on the development of $CD163^+$ and $SPP1^+$ TAMs, which are implicated in tumor progression. First, we analyzed the survival outcomes of over 11,000 patients from The Cancer Genome Atlas (TCGA) Pan-Cancer (PANCAN) database

(https://www.cancer.gov/tcga), categorizing them based on their *CD163* and *SPP1* expression levels. Our analysis corroborated the association of elevated *CD163* and *SPP1* levels with diminished survival in patients with solid cancer types. Subsequently, our goal was to construct regression models to evaluate how *HMOX1* expression predicts *CD163* and *SPP1* expression compared to other established TAM modifiers. We compiled a comprehensive list of known macrophage-polarizing stimuli and their representative marker genes from existing literature. This list included T cell markers *(CD4, CD8A)*, macrophage growth factor *CSF1*, a spectrum of pro- and anti-inflammatory cytokines *(TNF, IL1B, IL6, IL10)*, and the oxidative stress marker glutamate-cysteine ligase modifier subunit *(GCLM)*. Prior to modeling, we ensured the RNA count data for these genes, log2-transformed and batch-corrected (log2[count + 1]), conformed to a normal distribution. Linear regression models were then developed using *CD163* and *SPP1* as dependent variables, with the microenvironmental factors, including *HMOX1*, as independent variables or predictors (**Figure 1A**+**B**). The model for *CD163* expression demonstrated high accuracy (r^2 = 0.71), with *IL10* and *IL6* positively influencing and *IL1B* and *TNF* negatively influencing *CD163* levels, aligning with existing literature on cytokine impacts on *CD163* expression (32). The model for *SPP1*, though less robust (r^2 = 0.30), was still statistically significant. The negative correlation of *SPP1* expression with *CD8A* further supports the role of $SPP1^+$ TAMs in immune suppression (33). *HMOX1* was identified as a strong positive predictor for both TAM markers, suggesting that intratumoral heme exposure due to microhemorrhage may be a critical factor in fostering cancer-promoting TAMs.

Next, we aimed to identify TAM phenotypes in hemorrhagic tumors. We established an experimental model of therapy-induced hemorrhagic tumor necrosis by treating GFP-MC38 tumor-bearing mice with a single injection of the anti-CD40 agonist antibody FGK4.5 seven days after subcutaneous tumor cell injection (**Figure 1C**). We selected the MC38 colon adenocarcinoma model because these tumors are known to be sensitive to anti-CD40 immunotherapy (34). Three days after the anti-CD40 antibody injection, the tumors were collected for histology and genome-wide spatial analysis of mRNA expression. In tumor samples from two mice, H&E histology revealed extensive tumor necrosis with RBC extravasation into the necrotic areas (**Figure 1D**), thus confirming the presence of hemorrhagic tumor tissue. Then, we performed spatial gene expression analysis to achieve more detailed phenotyping; this analysis discriminated zones of remaining viable cancer cells surrounded by hemorrhagic necrosis, as

evidenced by the enrichment of RBC-derived mRNA *(Hbb-bs)* (**Figure 1E**). In these hemorrhagic regions, we found an increased *Cd68* signal, confirming macrophage infiltration, superimposed by upregulated expression of *Hmox1* and *Arg1*, the latter of which is the archetypal marker for procancerous and immunosuppressive TAMs in mice (22), similar to *CD163* and *SPP1* in human cancers.

Finally, since key characteristics of anti-inflammatory erythrophagocytic macrophages are driven by activated NRF2, we plotted an expression score of NRF2-activated genes. The results suggested high NRF2 activity in the *Cd68*^{high} *Hmox1*^{high}*Arg1*^{high} tumor regions (**Figure 1E**). In summary, these data indicate that hemorrhage enforces the accumulation of macrophages with a phenotype consistent with immunosuppressive and procancerous TAMs.

RBC and heme drive the generation of TAM-like macrophages with an immunocompromised phenotype

Experimentally manipulating the tumor microenvironment to study phenotype-driving factors poses substantial challenges. Hence, we examined macrophages within modifiable artificial tissue scaffolds based on Matrigel plug constructs, which we subcutaneously placed in mice (**Figure 2A**). In the first model, we focused on the effect of a hemorrhage on macrophage phenotypes. We enriched Matrigel with fibroblast growth factor (FGF), resulting in variable plug vascularization and hemorrhage. Seven days after subcutaneous injection, plugs were explanted, and blinded investigators classified them as non-hemorrhagic (white/gray appearance) or hemorrhagic (red/yellow appearance, indicating the presence of hemoglobin, heme, and bilirubin) (**Figure 2B**). For both conditions, flow cytometry revealed infiltration of CD11b^{+}F4/80^{+} macrophages. However, the degree of MHC class II expression was significantly lower in the hemorrhagic compared to the non-hemorrhagic plugs (**Figure 2C**). This observation suggests that macrophages accumulating in a hemorrhagic tissue microenvironment exhibit an immunocompromised phenotype.

In the second set of experiments, we focused on the specific role of RBC-derived heme as an inducer of this MHC class II^{low} macrophage phenotype by incorporating mouse RBCs (RBC-heme) or heme-depleted RBC ghosts into the Matrigel (**Figure 2D**). Again, we detected CD11b^{+}F4/80^{+} macrophages in both plug types. MHC class II expression was lower in the RBC-heme plugs (**Figure 2E**). In addition, multiplexed-fluorescence immunohistochemistry

demonstrated that the infiltrating macrophages in the RBC-heme plugs were HMOX1 positive and iron loaded, consistent with a post-erythrophagocytic state, which was observed at higher magnification by the visualization of ingested RBC remnants (**Figure 2F**, **Supplementary Figure 1A**). This suggests that erythrophagocytosis is the principal route of heme delivery into the cells. Compared to the heme concentration within RBCs (~18 mM), the cell-free hemoglobin and heme concentrations in the plugs were low (**Supplementary Figure 1B** and **1C**).

To further delineate whether these RBC-heme-transformed macrophages share the phenotypic features of procancerous TAMs, we recovered macrophages from collagenase-digested RBC-heme or RBC-ghost plugs with F4/80 antibody-coupled magnetic beads and performed single-cell RNA-sequencing (scRNA-seq) analysis (**Figure 3A**). We identified 6434 macrophages (**Figure 3B**) and functionally classified them using published gene sets for specific macrophage functions (35). This analysis assigned the seven Leiden clusters to four major functional groups: phagocytosis, oxidative stress, antigen presentation, and cell cycling (**Figure 3B**, **Supplementary Figure 1D**). The category distributions are consistent with the pathway score intensities per cell. The predominant effect of heme-containing RBCs compared to RBC-ghosts was the emergence of a large population of macrophages attributed to the oxidative stress state with high expression of NRF2 target genes and a reduction in cells designated for antigen presentation (**Figure 3C**, **Supplementary 1E**).

Heme-exposed macrophages in RBC-heme plugs were characterized by high expression of genes related to the metabolism of heme *(Hmox1)*, iron *(Slc40a1)*, and antioxidants *(Gclm*, *Prdx1)*. They also expressed the procancerous TAM markers *Arg1* and *Spp1* (**Figure 3D**). In contrast, MHC class II expression *(H2-Ab1, H2-Eb1)* was diminished within these macrophages. The different macrophage phenotypes in RBC-heme plugs versus ghost plugs were confirmed in independent experiments by RT–qPCR analysis of selected signature genes (**Figure 3E**). This data supports that heme exposure leads to the emergence of *Arg1*^{high}*Spp1*^{high} macrophages.

Finally, we projected the gene expression score defining the RBC-heme-induced *Arg1*^{high}*Spp1*^{high} oxidative stress macrophages into the spatial gene expression map of the hemorrhagic GFP-MC38 tumors. We found a high score intensity in the hemorrhagic necrosis zones around the viable cancer tissue remnants (**Figure 3F**). This supports the idea that the macrophages in our Matrigel scaffold model represent hemorrhage-associated TAMs.

Collectively, these data suggest that the sequence of RBC extravasation,

erythrophagocytosis, and intracellular heme signaling generates *Arg1*^{high}*Spp1*^{high} macrophages. These cells exhibit an NRF2-regulated antioxidant gene expression profile and attenuated immune function, sharing strong phenotypic characteristics with pro-cancerous TAMs. From this point forward, we refer to these macrophages as heme-TAMs.

Mixed cell-type spheroids support the generation and maintenance of heme-TAMs in an experimental tumor microenvironment

In the next step, we sought to develop a model to facilitate the generation and functional characterization of heme-TAMs in vitro. To do this, we tested whether treating bone marrow-derived macrophages (BMDMs) with heme in cell culture would transform them into heme-TAMs. Bulk RNA-sequencing (RNA-seq) (**Figure 4A**) revealed that heme exposure induced a *Hmox1*^{high}*Marco*^{high}*MHC class II*^{low} macrophage phenotype and strong expression of NRF2-regulated genes (**Figure 4B**). However, these cells showed weak expression of the TAM marker gene *Arg1*, indicating that heme treatment alone was insufficient to induce the full heme-TAM phenotype. Therefore, we explored whether additional tissue microenvironmental factors could synergize with heme. In a factorial study, we treated BMDMs with heme, MC38 colon adenocarcinoma cell culture supernatant, or a combination of both stimuli. Although neither of the two stimuli alone could fully induce the expression of *Arg1*, we found a strong synergistic effect (**Figure 4C**), suggesting that heme, in conjunction with factors provided by the tumor cell culture supernatant, serves as a potent signal for the generation of heme-TAMs.

Next, we established a three-dimensional culture of MC38 cancer cells mixed with heme-treated BMDMs in microwell plates to mimic the tumor microenvironmental TAM niche more accurately (**Figure 4D**). This procedure generated tumor spheroids with uniformly interspersed macrophages (**Figure 4E**). We profiled the transcriptome of macrophages within these spheroids using scRNA-seq 24 hours after spheroid formation. To test the robustness of heme as a TAM phenotype driver, we conducted a multiplexed experiment evaluating different macrophage pretreatments consisting of heme alone and combinations of heme with the classical M1-polarization stimuli IFNγ and LPS (**Figure 4F**). Macrophages were identified by *Ptprc* (CD45) expression (**Figure 4G**) and subjected to principal component analysis (PCA) based on the highly variable genes (**Figure 4H**, **Supplementary Figure 2A**). PC1 separated all heme-exposed

macrophages from cells treated solely with IFNγ or LPS, describing a dominant heme effect that superseded the impact of the proinflammatory stimuli. Analysis of all mRNA transcripts sorted by their weighted contribution to PC1 (PC1 loading) revealed that high expression of the TAM marker gene *Arg1*, NRF2 target genes (e.g., *Gstm1*), and TAM-associated matrix remodeling genes *(Mmp8, Mmp12)* was highly discriminative, as was suppression of MHC class II genes *(H2-Ab1*, *H2-Aa)*, *Cd74*, and *C1qa* (**Figure 4I**). Moreover, macrophages exposed to heme had higher expression levels of *Hmox1*, *Marco*, and the TAM marker *Spp1* (**Figure 4J**). Before conducting functional studies, we wanted to confirm the stability of the heme-TAM phenotype during extended spheroid culture. Therefore, we analyzed macrophages extracted from spheroids after four, eight, and ten days (**Supplementary Figure 2B** and **2C**). Based on expression data for *Marco*, *Arg1*, *Spp1*, *Cd74*, and *H2-Ab1*, the macrophage phenotype was remarkably stable (**Supplementary Figure 2D**).

In summary, we discovered that within the microenvironment of a spheroid culture system, heme exposure drives the transformation of macrophages into *Arg1*^{high}*Spp1*^{high} heme-TAMs with an enhanced matrix remodeling program and suppressed immune marker genes. Furthermore, heme-TAMs resist inflammatory rewiring by IFNγ and LPS.

Heme-TAMs prevent cancer cell apoptosis and drive growth, invasiveness, and metastasis

We next established an experimental framework to study the impact of heme-TAMs on growth and phenotype of cancer cells (**Supplementary Figure 3A**). In the first step, we cultured GFP-MC38 cells alone or with heme-treated macrophages in 96-well ultralow attachment plates. We monitored spheroid growth and apoptosis as GFP fluorescence and annexin V accumulation using a live cell imaging system. In the tumor cell-only spheroids, we observed a decay in GFP fluorescence after day 4, coinciding with increasing Annexin V fluorescence. In contrast, GFP fluorescence progressively increased without an Annexin V signal in the mixed cell-type spheroids (**Figures 5A** + **5B**). This was consistent with ATP measurements in single spheroids, which decreased after day 4 in the tumor cell-only spheroids but increased in the mixed cell-type spheroids (**Supplementary Figure 3B**). In a complementary setup, we cultured the same cells in microwell plates and collected numerous uniform spheroids for metabolic flux analysis at different time points. Again, on days 8 and 10 in culture, tumor cell-only spheroids decayed metabolically, while the mixed cell-type spheroids demonstrated an unaltered oxygen

consumption rate (OCR) throughout the 10-day culture period (**Supplementary Figure 3C**). Collectively, we observed that after four days, the size of GFP-MC38 spheroids regressed, and the tumor cells underwent apoptosis and decayed metabolically. In contrast, the presence of heme-TAMs within spheroids prevented apoptosis, supporting the extended growth of metabolically viable spheroids up to 10 days of culture.

To understand the impact of heme-TAMs on the cancer cell phenotype, we conducted multiplexed scRNA-seq experiments with tumor-only and mixed cell-type spheroids collected on days 4, 8, and 10 after formation. Before we processed the cells for scRNA-seq, we measured the size and fluorescence intensity of each analyzed spheroid by fluorescence microscopy to confirm the heme-TAM-supported spheroid growth (**Figure 5C**). After quality control and demultiplexing, macrophages were excluded from the analysis, and Leiden clustering of the tumor cells defined three clusters per condition (**Supplementary Figure 3D**). Cell density projections illustrate how the densities migrate through the UMAP across time, indicating that the transcriptome undergoes substantial changes (**Figure 5D**). We then used gene set enrichment analysis (GSEA) to extract the dominant functional characteristics for each cluster. The most significantly enriched pathways were related to proliferation, EMT, and the unfolded protein response (UPR) (**Supplementary Figure 3D**). An analysis of the proportion of tumor cells attributed to each cluster/functional category on days 4, 8, and 10 revealed that tumor cell spheroids were proliferative and in a state of EMT on day 4 but entering the UPR state afterward, with most cells projecting into the UPR cluster on days 8 and 10 (**Figure 5E).** This is consistent with the progressive apoptosis and metabolic decay of these spheroids. In contrast, tumor cells in the mixed spheroids were predominantly proliferative on day 4, transitioning into a stable state of proliferation and EMT. The expression of selected signature genes for proliferation, EMT, and UPR is highlighted in **Supplementary Figure 3E**.

EMT is a physiological process that enhances invasiveness and is thus a key determinant of cancer progression (36). In mixed spheroids, heme-TAMs dramatically increased the invasion of GFP-MC38 tumor cells, which progressed for more than four days after the spheroids were embedded into an extracellular matrix (**Figure 5F** and **5G**). The ultimate disease correlate of EMT is cancer metastasis. Consequently, we collected spheroids five days post-formation and injected approximately 750 intravenously into mice. Three weeks after injection, we observed

substantially more extensive pulmonary metastasis in mice injected with mixed spheroids than those injected with tumor cell spheroids (**Figure 5H**). Taken together, our findings suggest that heme-TAMs promote tumor cell proliferation and EMT, fostering an invasive and highly metastatic cancer phenotype.

Heme-TAMs resist tumoricidal transformation by IFNγ

Inflammatory macrophage activation in the tumor microenvironment is a critical component of the antitumor immune response and an emerging therapeutic concept (25). So far, we have focused our functional studies on the procancerous effects of heme-TAMs, ignoring the comparison with other macrophage polarization states. We mixed GFP-MC38 cells with BMDMs that were either untreated, representing an undetermined polarization state, or pretreated with heme, IFNγ, or heme + IFNγ, and monitored spheroid growth and regression over time (**Figure 6A**). Our findings showed that untreated macrophages had a tumoricidal effect immediately after spheroid formation, which IFNγ further enhanced. In contrast, heme-pretreated BMDMs were not tumoricidal and instead promoted tumor cell growth, as seen before. This pattern of spheroid growth was not altered when heme-TAMs were treated with IFNγ, suggesting that heme-TAMs were resistant to the tumoricidal effect of IFNγ. This is consistent with a bulk RNA-seq experiment of BMDMs, which demonstrated that heme substantially repressed the IFNγ-induced transcriptional response. This repression included *Cxcl9*, *Cxcl10*, and *Cxcl11*, which have been identified as prognostically favorable markers of an antitumor microenvironment (18) (**Figure 6B**).

We repeated the identical experiment using scRNA-seq as a readout to obtain more in-depth insight into the effects of differently polarized BMDMs on MC38 tumor cells. We stimulated BMDMs with heme, IFNγ, or heme + IFNγ, and measured mitochondrial function and the glycolytic rate of BMDMs using a Seahorse metabolic flux analyzer to confirm maintained viability (**Supplementary Figure 4A**). Spheroids were then generated and cultured in microwell plates. Before spheroids were dissociated and labeled for multiplexing, the size and fluorescence intensity of each spheroid were quantified on day 9. This data confirmed the enhanced tumoricidal activity of IFNγ-treated BMDMs (red violin plot) compared to untreated BMDMs and that heme exposure made macrophages resistant to the induction of tumoricidal activity by IFNγ (**Figure 6C**). Then, an equal number of cells per condition was processed for scRNA-seq, and a

UMAP of 6808 MC38 tumor cells color-coded for conditions was created (**Figure 6D**); based on *Ptprc* (CD45) expression, macrophages were excluded from this analysis (**Supplementary Figure 4B**). Subsequently, we used Leiden clustering to define three tumor cell clusters, assigning each cell to a functional state representing proliferation, EMT, or UPR (**Figure 6E**, **Supplementary Figure 4C** and **4D**). In spheroids without macrophages, tumor cells were mainly in the UPR state. Most tumor cells were proliferative in spheroids with untreated BMDMs or IFNγ-treated BMDMs (**Figure 6E**). This is a sequela of the tumoricidal macrophage activity, which triggers the compensatory proliferation of the remaining tumor cells. In contrast, in spheroids containing heme-pretreated BMDMs, most tumor cells were in the EMT state, irrespective of IFNγ treatment.

To integrate the gene expression analysis with the information obtained by the size and fluorescence intensity quantification of the spheroids, we plotted normalized cell densities (**Figure 6F**) alongside the pathway score intensities for UPR, proliferation, and EMT (**Figure 6G**). The data visualize that a very high cell density projects on the UMAP area representing EMT in the spheroids containing heme-TAMs, irrespective of whether the macrophages have been treated with IFNγ. This allowed us to discern that heme abrogates the tumoricidal activity of macrophages, supporting the growth of large cancer spheroids in a persistent EMT state.

We validated our findings in vivo by assessing the metastatic potential of the different spheroids in immunodeficient mice. Three weeks after intravenous injection of an equal number of spheroids per condition and mouse (approximately 750), pulmonary metastases were sparse in mice inoculated with spheroids containing untreated or IFNγ-treated BMDMs. In contrast, we found extensive metastatic disease in the mice injected with spheroids containing either heme-treated or heme + IFNγ-treated BMDMs (**Figure 6H**, **Supplementary Figure 4E**). These data confirm that heme exposure undermines the activity of IFNγ to induce tumoricidal activity in TAMs.

To generalize our findings obtained with MC38 cells, we evaluated the antitumoral activity of heme-pretreated BMDMs using mCherry-4T1 mammary carcinoma cells and GL-261 Luc glioma cells (**Supplementary Figure 4F**). These tumor cell lines were selected for their representation of different cancer types and their capacity to form spheroids with BMDMs,

which was defined in pilot experiments. As with MC38 cells, heme-pretreated BMDMs fostered tumor growth and resistance to IFNγ with both tumor cell lines. Our data demonstrate that heme exposure in macrophages generates a dominant signal attenuating tumoricidal function and promoting cancer progression.

Heme signaling progresses via NRF2 to promote heme-TAM transformation, tumor cell growth, invasiveness, and metastasis

Heme-activation of NRF2 is a strong anti-inflammatory signal in macrophages (27), and the analyses presented above indicate that the expressed transcriptome in heme-TAMs is consistently enriched for NRF2 target genes. Therefore, we delineated the role of NRF2 in the heme-TAM transformation process by performing a series of experiments with *Nrf2*-knockout (KO) BMDMs, leading to a locked NRF2-off state and macrophages with KO of the cytoplasmic NRF2 capture protein KEAP1, leading to a locked NRF2-on state, irrespective of the presence or absence of heme (**Figure 7A**). We found that *Nrf2* KO interrupted the synergistic effects of heme and MC38 cell-conditioned medium on *Arg1* mRNA expression in 2D BMDM cultures (**Figure 7B**). In mixed cell-type spheroids, *Nrf2* KO in macrophages reversed the growth-promoting effect of heme-pretreated BMDMs on MC38 cancer cells. Notably, heme-pretreated *Nrf2* KO BMDMs had paradoxically enhanced tumoricidal activity, consistent with the unchained proinflammatory function of heme without anti-inflammatory NRF2 (**Figure 7C** + **7D**). Our findings show that NRF2 signaling is essential for macrophages to acquire the heme-TAM phenotype.

Next, to demonstrate that activated NRF2 is sufficient to drive heme-TAM transformation, we analyzed *Keap1* KO macrophages. In a multiplexed scRNA-seq experiment comparing the gene expression profiles of untreated wild-type (WT) BMDMs, heme-treated WT BMDMs, and untreated *Keap1* KO BMDMs, the expression of canonical myeloid markers was similar in both WT and *Keap1* KO BMDMs, excluding divergent differentiation trajectories of macrophages in response to enhanced NRF2 activity (**Figure 7E**). However, there were also differences, explaining the divergent UMAP positions of the three cell populations. For example, heme-treated BMDMs displayed uniquely high expression of *Hmox1*. In contrast, heme-pretreated WT BMDMs and *Keap1* KO BMDMs shared increased expression of the NRF2 target genes *Gclm*, *Gsr*, *Slc7a11*, and *Marco*. With the same scRNA-seq data, we also performed PCA, which is more sensitive for detecting similarities among samples than UMAP-based

dimensionality reduction. This analysis revealed that the heme-treated WT BMDMs and the untreated *Keap1* KO BMDMs were largely overlapping and separate from the untreated WT BMDMs (**Figure 7F**). The differentially expressed genes defining PC1 and PC2 were highly enriched for NRF2 targets. This confirmed that heme activation of NRF2 is the dominant phenotype driver of heme-TAMs and that constitutive NRF2 activation is sufficient to mimic this phenotype. In line with these gene expression results, we observed that *Keap1* KO BMDMs fully replicated the growth- and matrix invasion-promoting effects of heme-TAMs in MC38 cancer cell spheroids (**Figure 8A** + **8B**).

To validate the procancerous effect of NRF2 activity in TAMs in vivo, we injected GFP-MC38 spheroids containing macrophages with locked NRF2-off or locked NRF2-on intravenously into mice (**Figure 8C**). We used immunodeficient *Rag2*$^{-/-}\gamma c^{-/-}$ mice for these studies to avoid interference with endogenous immune responses. Three weeks after intravenous injection of an equal number of spheroids per condition and mouse (approximately 750 spheroids), we observed much more extensive metastatic disease in the mice injected with spheroids containing macrophages with a locked NRF2-on state, irrespective of whether NRF2 was activated by heme or constitutively active due to the genetic absence of *Keap1*. In contrast, spheroids containing macrophages with a locked NRF2-off state had low metastatic potential, irrespective of whether the macrophages had been pretreated with heme (**Figure 8C**, **Supplementary Figure 5A**, **Supplementary Figure 5B, Supplementary Figure 5C**).

Heme NRF2 signaling in hematopoietic cells promotes resistance to immunotherapy

Finally, we aimed to investigate whether hemorrhage-NRF2 signaling in macrophages could also undermine macrophage reprogramming-based immunotherapy. We first examined whether a hemorrhagic microenvironment changes the transcriptional response of macrophages to agonistic anti-CD40 antibodies. To investigate this, we used our Matrigel scaffold model with RBC-heme or RBC-ghost incorporated (**Figure 9A**). Seven days after plug placement, we treated the mice with agonistic anti-CD40 antibody. Twenty-four hours later, we detected less expression of *Cxcl9* and *Cxcl10* in F4/80+ macrophages of the RBC-heme-enriched plugs, while Hmox1 was superinduced (**Figure 9B**). The CD40-triggered *Cxcl9* and *Cxcl10* response was significantly more intense when the RBC-heme plugs were placed in conditional *Nrf2* KO compared to *Nrf2* WT mice (**Figure 9C**). This is consistent with the assumption that heme-signaling through NRF2

prompted resistance of TAMs to therapeutic reprogramming by anti-CD40 antibodies. To explore the potential therapeutic implications of this finding, we assessed whether active NRF2 within leukocytes of the tumor microenvironment is sufficient to induce resistance to anti-CD40 therapy. We injected GFP-MC38 tumor cells subcutaneously into both flanks of WT mice and those with conditional *Keap1* KO in leukocytes (**Figure 9D**). After seven days, the mice were treated with anti-CD40 antibody, and three days later, the tumors were recovered for necrosis assessment. On visual inspection of tissue in situ, the tumors in WT animals displayed dark discoloration, providing evidence of extensive tumor necrosis and diminished GFP fluorescence intensity. In contrast, tumors in conditional *Keap1* KO animals looked viable post-treatment with very bright GFP fluorescence (**Figure 9E**). We also quantified tumor GFP fluorescence intensity post-anti-CD40 treatment and found significantly higher fluorescence of the tumors grown in the conditional *Keap1* KO animals (**Figure 9F**). These data were substantiated by histology, which revealed extensive tumor necrosis and loss of GFP immunoreactivity in anti-CD40-treated WT mice but not in KO animals (**Figure 9E**).

To validate the negative interference of heme-NRF2 signaling with CD40-mediated immunotherapy, we performed experiments with *Nrf2* KO models. Initially, we used our mixed cell-type spheroid model, which allows us to control heme exposure, NRF2 status, and CD40 activation of macrophages precisely. Live cell microscopy-based analysis of spheroid growth revealed that antibody-mediated crosslinking of CD40 on macrophages induced vigorous tumoricidal activity, leading to rapid spheroid regression. This effect was not affected by NRF2 status. However, heme pretreatment of WT, not *Nrf2* KO macrophages, abolished the CD40-induced tumoricidal activity, leading to massive spheroid growth (**Figure 9G**). These in vitro findings were recapitulated when we injected the spheroids post-formation intravenously into mice. In the first metastasis experiment, we confirmed that CD40-crosslinking on TAMs reduced metastasis formation. A second experiment confirmed that more metastases form with heme-TAMs and that CD40-crosslinking does not impact metastasis formation in this scenario. In contrast, when we used *Nrf2* KO macrophages in the third experiment, there was no apparent pro-metastasis effect of heme, and the tumoricidal activity of CD40-crosslinking was restored (**Figure 9H**).

Finally, we used the subcutaneous MC38 tumor model. We hypothesized that the tumor hemorrhage, which is consistently induced by anti-CD40 therapy, might attenuate the immunotherapeutic response to a second antibody injection by an NRF2-dependent mechanism. Consistent with this hypothesis, we found smaller tumors with barely detectable GFP fluorescence 48 hours after the second antibody injection in mice with a conditional KO of *Nrf2* in leukocytes compared to WT mice (**Figure 9I**). Collectively, these data suggest that hemorrhage – through heme-activated NRF2 in macrophages of the tumor microenvironment – undermines the anti-CD40 antibody therapeutic response.

DISCUSSION

Hemorrhage occurs ubiquitously in many solid cancers but has not been considered a biological modifier of cancer biology. Recognizing the quintessential functions of macrophages in the disposal of RBCs, we discovered in this study a trajectory that connects intratumoral hemorrhage to the creation of procancerous TAMs. We found that erythrophagocytosis in the tumor microenvironment initiates this trajectory, elevating intracellular heme levels and activating downstream NRF2 signaling. This prompts a transformative phenotype shift in macrophages, enhancing regenerative capacities while suppressing immune functions. These hemorrhage-derived TAMs drive cancer growth, tissue invasion, and resistance to CD40-agonistic immunotherapy.

The role of macrophage polarization within the tumor microenvironment as a determinant of cancer progression, immune regulation, and treatment outcomes is well-established. However, the traditional M1 versus M2 polarization dichotomy has not consistently explained prognostic variability. A comprehensive gene expression analysis across numerous human solid cancer types recently revealed a stronger predictive association with a polarity defined by *CXCL9* and *SPP1* (18). High expression of the IFNγ response gene *CXCL9* in TAMs corresponded to a favorable prognosis. In contrast, a high *SPP1* and low *CXCL9* expression pattern was associated with poor prognosis and weakened response to immunotherapy. Our regression modeling of cancer mRNA expression data from over 11,000 patients in the TCGA PANCAN database suggested that heme exposure, measured by *HMOX1* expression, strongly predicts *SPP1*. In line with this finding, our experiments showed that heme-NRF2 signaling

reproduced the *Spp1*^{high}/*Cxcl9*^{low} poor prognosis phenotype in mouse BMDMs, reinforcing that hemorrhage might be a universal and clinically important TAM polarization factor. Thus, systematic studies are warranted to explore the relationship between spontaneous or treatment-induced hemorrhage, tumor microenvironmental heme exposure, and disease outcomes in various cancers.

Heme-activated NRF2 endows TAMs with an immunosuppressive phenotype, promoting cancer cell EMT, matrix invasion, and high metastatic potential while impairing tumoricidal activity. These effects of NRF2 activation in TAMs involve a combination of intrinsic and extrinsic mechanisms. Intrinsic mechanisms lock TAMs into an immune-suppressed state, providing resistance against macrophage activation induced by IFNγ and agonistic anti-CD40 antibodies. In contrast, extrinsic mechanisms offer anti-apoptotic and pro-invasion signals to cancer cells. Collectively, it is likely that NRF2-educated TAMs adversely affect outcomes of solid cancers. Further investigation has to establish the molecular nature of the mechanisms transforming macrophage functions downstream of NRF2.

Tumor cell-intrinsic NRF2 has been comprehensively studied and is known to play dual roles in tumorigenesis, acting both as a tumor suppressor and promoter, depending on the context and disease stage (37–39). NRF2 primarily supports redox homeostasis by activating genes involved in antioxidant enzyme production and detoxification proteins, offering a safeguard against cancer development (40–43). However, persistent NRF2 activation in established cancer cells, often resulting from mutations in *KEAP1* or *NRF2*, promotes tumor cell survival, growth, and resistance to therapy (44, 45). Less is known about the regulators of NRF2 activity in cells of the cancer microenvironment and how NRF2 activation there may feed back on cancer progression and anti-cancer immune responses. NRF2 induces extensive transcriptional and metabolic reprogramming in myeloid cells (46). Beyond attenuating intrinsic tumoricidal functions, as our studies show, elevated NRF2 activity in macrophages shapes an immunosuppressive milieu that impairs cytotoxic T-cell functionality and fosters immune tolerance through Treg recruitment (47, 48). Concurrently, NRF2 activation modulates extracellular matrix composition (49), potentially promoting tumor invasiveness. Furthermore, heme exposure and NRF2 activation intensify glycolysis and lactate production (50–53), possibly underpinning a harmful metabolic coupling between TAMs and cancer cells (54–56).

Given its chemistry, the oxidant heme has the potential to broadly activate NRF2 across cell types and tissues (57). However, physiological mechanisms, such as hemoglobin coordination and packaging within the RBC membrane, RBC antioxidant metabolites, and extracellular scavenger proteins, effectively shield tissue environments against oxidative impact from heme (31, 57, 58). Instead, the hemorrhage-triggered wound healing response recruits macrophages (59), which have the unique ability to recognize and ingest damaged RBCs and heme-protein complexes (60), allowing them to shuttle heme toward a system capable of safely degrading and reutilizing its components (61). In this context, NRF2 activation forms part of the adaptive response of macrophages (27, 62–65). Thus, RBC-heme may be considered a uniquely macrophage-specific NRF2 activator in the hemorrhagic tumor microenvironment.

Our findings also align with previous observations linking HMOX1-expressing macrophages in the tumor microenvironment to cancer progression and unfavorable disease outcomes (66–68). Notably, our findings connect this association to a pathophysiological pathway initiated by spontaneous or therapy-induced intratumoral hemorrhage. HMOX1 is most strongly induced in macrophages among heme-induced genes and, therefore, a perfect marker for this process. Nevertheless, in our studies, NRF2 activation was sufficient to transmit TAM reprogramming, with no apparent functional role of the marker HMOX1 in this process. We learned to interpret studies of HMOX1 inhibition and knockout models very cautiously. In the absence of HMOX1, cells are exceedingly vulnerable when exposed to heme, and some effects may reflect the consequences of cell depletion in heme-rich microenvironments rather than more specific signaling functions of the enzyme or its downstream metabolites (57).

Overall, our discoveries potentially explain the limited effectiveness of conventional therapies and immunotherapies in overtly hemorrhagic tumors, such as gliomas (69), and the progressive immunoresistance observed across various malignancies (70). Further research could develop novel therapies that harness NRF2 signaling in macrophages to boost cancer immunity and overcome treatment resistance.

METHODS

Additional and detailed protocols and reagents are provided in the Supplementary Methods.

Mouse strains and breeding

C57BL/6J (JAX™ strain) mice were obtained from Charles River Laboratories. To generate *tdTomato*$^{+}$ macrophages, *Vav-Cre* mice, obtained from the Swiss Immunological Mouse repository (SwImMR), were bred with *Ai14*^{tdTomato} mice (The Jackson Laboratory). *Conditional Keap1 knockout mice: Keap1*$^{tm2.Mym}$ (71) mice were obtained from RIKEN BRC and crossed with Vav-Cre mice. *Conditional Nrf2 knockout mice:* C57BL/6-*Nfe2l2tm1.1Sred/SbisJ* (*Nrf2*^{flox}) (72, 73) mice were obtained from Jackson laboratories and crossed with *Vav-Cre* mice. Control littermates without the Cre driver were used for experiments involving these mouse strains. *Nrf2* KO and WT littermates were obtained from Professor Yuet Wai Kan (University of California, San Francisco). *Rag2*$^{-/-}\gamma c^{-/-}$ mice were obtained from SwImMR. For all studies, mice were randomly allocated to treatment groups, and the investigators were blinded to allocation during experiments and outcome assessment.

Cell lines and primary BMDM cultures

Methods for tumor cell and BMDM cultures are provided in the Supplementary Methods.

Heme preparation for cell culture

Hemin (heme-chloride) was obtained from Frontier Scientific (Newark). Batches were tested endotoxin-free and prepared as heme-albumin for cell treatments as described (60).

3D tumor spheroid production, culture, and analysis

Single-spheroid culture

5×10^3 GFP-MC38 cells, 2.5×10^3 mCherry-4T1 cells, or 5×10^3 GL261-Luc cells ± BMDMs (at a 1:1 ratio) were seeded in 100 µl tumor cell culture medium in 96-well Ultralow Attachment Plate PrimeSurface® 3D Culture Spheroid plates (S-BIO). M-CSF (100 ng/ml) was added to all spheroid cultures irrespective of the addition of BMDMs to control for the cytokine effect. For live cell apoptosis imaging, Annexin V red (Sartorius) was added to the medium, as instructed by the manufacturer.

Multispheroid culture in microwell plates

GFP-MC38 cells *(*5 x 10^4) ± BMDMs (at a 1:1 ratio) were seeded in 800 µl of tumor cell medium with M-CSF (100 ng/ml) in a 24-well SphericalPlate® 5D microwell (Axonlab). 800 µl of fresh culture cell medium was added on day 3.

Quantification of spheroid growth and invasion

Single spheroids were imaged with an IncuCyte S3 instrument (Sartorius). The area and fluorescence intensities of the images were measured using the IncuCyte Spheroid Software Module (Sartorius). Data are reported as spheroid fluorescence intensity integrated across the spheroid area (for tumor cells expressing a fluorescent protein) or as spheroid area. For the spheroid invasion assay, a mask based on the invading cell area was created automatically with the IncuCyte Spheroid Software Module. Multispheroids were scanned using a Zeiss Axio Observer Z1 microscope. The spheroid area was quantified manually in QuPath (74) (v0.3.0), and fluorescence intensity was measured using QuPath's intensity feature plugin. The spheroids were detected in the EGFP/FITC channel using a set pixel size of 1.26 µm.

Mouse models

Subcutaneous Matrigel plug model in mice

350 µl Matrigel mixture was injected subcutaneously into the flanks of anesthetized (intraperitoneal injection of ketamine (80 mg/kg), xylazine (16 mg/kg), acepromazine (3 mg/kg)) C57BL/6J mice using a 24-G needle. After seven days, mice were euthanized, and plugs were removed for downstream analysis. For anti-CD40 antibody experiments, the mice were treated intravenously on day 7 with an agonistic anti-CD40 antibody (20 mg/kg, InVivoPlus, clone FGK4.5) or an isotype control antibody.

Lung metastasis model in mice

Approximately 750 spheroids were collected from microwell plates (equal to the content of one macro well) and injected intravenously into the tail vein of C57BL/6J or *Rag2*$^{-/-}$*γc*$^{-/-}$ mice. Three weeks post-injection, the lungs of anesthetized mice were perfused with PBS through the right ventricle and the trachea and collected for whole organ fluorescence imaging with a Zeiss Discovery V8 stereomicroscope and histology. For the metastasis experiments shown in Figure 9H, metastasis were manually counted to enhance sensitivity and specificity in the low disease burden range to assess the effects of anti-CD40 treatment.

Tumor growth model in mice

Once confluent, GFP-MC38 tumor cells were harvested using 5 mM EDTA (Gibco) (4 min at 37°C) and washed twice in PBS. MC38 cells (2 x 10^6) in culture medium were mixed with Geltrex (Thermo Fisher) and injected subcutaneously into the mouse flanks. Agonistic anti-CD40 treatment (20 mg/kg, InVivoPlus, clone FGK4.5) or an isotype control antibody was administered intravenously as indicated. Mice were euthanized, and tumors were collected two or three days after antibody administration. GFP fluorescence was measured immediately, and tumors were then fixed in formalin (10%) and stored at room temperature.

Sequencing-based workflows and data analysis

We used the 10X workflows for scRNA-seq (Chromium Next GEM Single Cell 3' v3.1) and spatial RNA-seq (Visium CytAssist Spatial Gene Expression for FFPE). Ready-made libraries were sequenced at the Functional Genomics Center Zurich (FGCZ) on an Illumina NovaSeq 6000 system. Downstream analysis was performed in Python (version 3.8.6) with Scanpy (1.7.0) (75). Details of sample preparation and data analysis are provided on an experiment-by-experiment basis in the Supplementary Methods.

Statistics

Data plotting and statistical analysis were performed with Prism 9 (GraphPad) and JMP 15 (SAS). We used ANOVA with Tukey–Kramer posttest to account for multiple comparisons and t-tests (two-tailed) or Wilcoxon tests, as indicaMethods the figure legends. All data points are displayed in box plots to visualize the data distribution. Analysis of sequencing data is described in the Supplementary Methods section.

Study approval

All animal experiments were performed according to animal experimentation licenses as approved by the Swiss Federal Veterinary Office.

Data and code availability

Sequencing data are publicly available (GEO accession code GSE237612). Detailed information is provided on an experiment-by-experiment basis in the Supplementary Methods. A file containing supporting data values is provided as a supplementary file.

Author contributions

DJS designed the study, performed experiments, analyzed the data, and wrote the manuscript. NSL performed the mouse experiments and analyzed the data. LB performed the RNA sequencing experiments and analyzed the data. KH performed the histological experiments. RMB performed experiments, analyzed data, and reviewed the manuscript. RH acquired the animal experimentation licenses, performed confocal microscopy, and designed the graphical abstract. ED analyzed the sequencing data. FV designed the study, performed experiments, analyzed data, and wrote the manuscript.

Conflict-of-interest statement

The authors have declared that no conflict of interest exists.

Acknowledgments

We thank G. Christofori, L. Borsig, and J. Vom Berg at the University of Zurich for providing GFP-MC38, mCherry-4T1, and GL-261-Luc cells. We thank Larissa Imhof and Tobias Fischer for spheroid image analysis.

Funding

Swiss National Science Foundation (project grant 310030_197823 to DJS, 310030_201202/1 to FV), Swiss Federal Commission for Technology and Innovation (project 19300.1 PFLS-LS to DJS), Vontobel Foundation (to FV).

REFERENCES

1. Pittet MJ, Michielin O, Migliorini D. Clinical relevance of tumour-associated macrophages. *Nat Rev Clin Oncol*. 2022;19(6):402–421.

2. Sica A, Mantovani A. Macrophage plasticity and polarization: in vivo veritas. *J Clin Invest*. 2012;122(3):787–795.

3. Salmon H, et al. Host tissue determinants of tumour immunity. *Nat Rev Cancer*. 2019;19(4):215–227.

4. Lazarov T, et al. Physiology and diseases of tissue-resident macrophages. *Nature*. 2023;618(7966):698–707.

5. Molgora M, Colonna M. Turning enemies into allies—reprogramming tumor-associated macrophages for cancer therapy. *Med*. 2021;2(6):666–681.

6. Cassetta L, Pollard JW. Targeting macrophages: therapeutic approaches in cancer. *Nat Rev Drug Discov*. 2018;17(12):887–904.

7. Chen S, et al. Tumor-associated macrophages are shaped by intratumoral high potassium via Kir2.1. *Cell Metab*. 2022;34(11):1843–1859.e11.

8. Bohn T, et al. Tumor immunoevasion via acidosis-dependent induction of regulatory tumor-associated macrophages. *Nat Immunol*. 2018;19(12):1319–1329.

9. Brand A, et al. LDHA-Associated Lactic Acid Production Blunts Tumor Immunosurveillance by T and NK Cells. *Cell Metab*. 2016;24(5):657–671.

10. Colegio OR, et al. Functional polarization of tumour-associated macrophages by tumour-derived lactic acid. *Nature*. 2014;513(7519):559–563.

11. Henze A-T, Mazzone M. The impact of hypoxia on tumor-associated macrophages. *J Clin Invest*. 2016;126(10):3672–3679.

12. De Palma M, Biziato D, Petrova TV. Microenvironmental regulation of tumour angiogenesis. *Nat Rev Cancer*. 2017;17(8):457–474.

13. Devalaraja S, et al. Tumor-Derived Retinoic Acid Regulates Intratumoral Monocyte Differentiation to Promote Immune Suppression. *Cell*. 2020;180(6):1098–1114.e16.

14. Wu J-Y, et al. Cancer-Derived Succinate Promotes Macrophage Polarization and Cancer Metastasis via Succinate Receptor. *Mol Cell*. 2020;77(2):213–227.e5.

15. Pollard JW. Tumour-educated macrophages promote tumour progression and metastasis. *Nat Rev Cancer*. 2004;4(1):71–78.

16. Tam WL, Weinberg RA. The epigenetics of epithelial-mesenchymal plasticity in cancer. *Nat Med*. 2013;19(11):1438–1449.

17. Su S, et al. A positive feedback loop between mesenchymal-like cancer cells and macrophages is essential to breast cancer metastasis. *Cancer Cell*. 2014;25(5):605–620.

18. Bill R, et al. CXCL9:SPP1 macrophage polarity identifies a network of cellular programs that control human cancers. *Science*. 2023;381(6657):515–524.

19. Gao W, et al. SPP1 is a prognostic related biomarker and correlated with tumor-infiltrating immune cells in ovarian cancer. *BMC Cancer*. 2022;22(1):1367.

20. Komohara Y, Jinushi M, Takeya M. Clinical significance of macrophage heterogeneity in human malignant tumors. *Cancer Sci*. 2014;105(1):1–8.

21. Qi J, et al. Single-cell and spatial analysis reveal interaction of FAP+ fibroblasts and SPP1+ macrophages in colorectal cancer. *Nat Commun*. 2022;13(1):1742.

22. Rodriguez PC, et al. Arginase I production in the tumor microenvironment by mature myeloid cells inhibits T-cell receptor expression and antigen-specific T-cell responses. *Cancer Res*. 2004;64(16):5839–5849.

23. Heusinkveld M, van der Burg SH. Identification and manipulation of tumor associated macrophages in human cancers. *J Transl Med*. 2011;9:216.

24. Beatty GL, et al. CD40 agonists alter tumor stroma and show efficacy against pancreatic carcinoma in mice and humans. *Science*. 2011;331(6024):1612–1616.

25. Engblom C, Pfirschke C, Pittet MJ. The role of myeloid cells in cancer therapies. *Nat Rev Cancer*. 2016;16(7):447–462.

26. Watanabe S, et al. The role of macrophages in the resolution of inflammation. *J Clin Invest*. 7 2019;129(7):2619–2628.

27. Pfefferlé M, et al. Hemolysis transforms liver macrophages into antiinflammatory erythrophagocytes. *J Clin Invest*. 2020;130(10):5576–5590.

28. Humar R, Schaer DJ, Vallelian F. Erythrophagocytes in hemolytic anemia, wound healing, and cancer. *Trends Mol Med*. 2022;28(11):906–915.

29. Olonisakin TF, et al. Stressed erythrophagocytosis induces immunosuppression during sepsis through heme-mediated STAT1 dysregulation. *J Clin Invest*. 2021;131(1):e137468.

30. Schaer CA, et al. Constitutive endocytosis of CD163 mediates hemoglobin-heme uptake and determines the noninflammatory and protective transcriptional response of macrophages to hemoglobin. *Circ Res*. 2006;99(9):943–950.

31. Vallelian F, Buehler PW, Schaer DJ. Hemolysis, free hemoglobin toxicity, and scavenger protein therapeutics. *Blood*. 2022;140(17):1837–1844.

32. Buechler C, et al. Regulation of scavenger receptor CD163 expression in human monocytes and macrophages by pro- and antiinflammatory stimuli. *J Leukoc Biol*. 2000;67(1):97–103.

33. Klement JD, et al. An osteopontin/CD44 immune checkpoint controls CD8+ T cell activation and tumor immune evasion. *J Clin Invest*. 2018;128(12):5549–5560.

34. Siwicki M, et al. Resident Kupffer cells and neutrophils drive liver toxicity in cancer immunotherapy. *Sci Immunol*. 2021;6(61):eabi7083.

35. Sanin DE, et al. A common framework of monocyte-derived macrophage activation. *Sci Immunol*. 2022;7(70):eabl7482.

36. Tiwari N, et al. EMT as the ultimate survival mechanism of cancer cells. *Semin Cancer Biol*. 2012;22(3):194–207.

37. Menegon S, Columbano A, Giordano S. The Dual Roles of NRF2 in Cancer. *Trends Mol Med*. 2016;22(7):578–593.

38. Pillai R, et al. NRF2: KEAPing Tumors Protected. *Cancer Discov*. 2022;12(3):625–643.

39. Rojo de la Vega M, Chapman E, Zhang DD. NRF2 and the Hallmarks of Cancer. *Cancer Cell*. 2018;34(1):21–43.

40. Itoh K, et al. Keap1 represses nuclear activation of antioxidant responsive elements by Nrf2 through binding to the amino-terminal Neh2 domain. *Genes Dev*. 1999;13(1):76–86.

41. Suzuki T, et al. Environmental pollutants and the immune response. *Nat Immunol*. 2020;21(12):1486–1495.

42. Westcott PMK, et al. The mutational landscapes of genetic and chemical models of Kras-driven lung cancer. *Nature*. 2015;517(7535):489–492.

43. Satoh H, et al. Nrf2-deficiency creates a responsive microenvironment for metastasis to the lung. *Carcinogenesis*. 2010;31(10):1833–1843.

44. Homma S, et al. Nrf2 enhances cell proliferation and resistance to anticancer drugs in human lung cancer. *Clin Cancer Res*. 2009;15(10):3423–3432.

45. DeNicola GM, et al. Oncogene-induced Nrf2 transcription promotes ROS detoxification and tumorigenesis. *Nature*. 2011;475(7354):106–109.

46. Kobayashi EH, et al. Nrf2 suppresses macrophage inflammatory response by blocking proinflammatory cytokine transcription. *Nat Commun*. 2016;7:11624.

47. Sha LK, et al. Loss of Nrf2 in bone marrow-derived macrophages impairs antigen-driven CD8+ T cell function by limiting GSH and Cys availability. *Free Radical Biology and Medicine*. 2015;83:77–88.

48. Yeang HXA, et al. Loss of transcription factor nuclear factor-erythroid 2 (NF-E2) p45-related factor-2 (Nrf2) leads to dysregulation of immune functions, redox homeostasis, and intracellular signaling in dendritic cells. *J Biol Chem*. 2012;287(13):10556–10564.

49. Hiebert P, et al. Nrf2-Mediated Fibroblast Reprogramming Drives Cellular Senescence by Targeting the Matrisome. *Dev Cell*. 2018;46(2):145–161.e10.

50. Bories GFP, et al. Macrophage metabolic adaptation to heme detoxification involves CO-dependent activation of the pentose phosphate pathway. *Blood*. 2020;136(13):1535–1548.

51. Hawkins KE, et al. NRF2 Orchestrates the Metabolic Shift during Induced Pluripotent Stem Cell Reprogramming. *Cell Rep*. 2016;14(8):1883–1891.

52. Fu J, et al. Hyperactivity of the transcription factor Nrf2 causes metabolic reprogramming in mouse esophagus. *J Biol Chem*. 2019;294(1):327–340.

53. Ryan DG, et al. Nrf2 activation reprograms macrophage intermediary metabolism and suppresses the type I interferon response. *iScience*. 2022;25(2):103827.

54. Colbert LE, et al. Tumor-resident Lactobacillus iners confer chemoradiation resistance through lactate-induced metabolic rewiring. *Cancer Cell*. 2023;41(11):1945–1962.e11.

55. Faubert B, et al. Lactate Metabolism in Human Lung Tumors. *Cell*. 2017;171(2):358–371.e9.

56. Whitaker-Menezes D, et al. Evidence for a stromal-epithelial “lactate shuttle” in human tumors: MCT4 is a marker of oxidative stress in cancer-associated fibroblasts. *Cell Cycle*. 2011;10(11):1772–1783.

57. Vallelian F, et al. Proteasome inhibition and oxidative reactions disrupt cellular homeostasis during heme stress. *Cell Death Differ*. 2015;22(4):597–611.

58. Galea I, et al. Haptoglobin Treatment for Aneurysmal Subarachnoid Hemorrhage: Review and Expert Consensus on Clinical Translation. *Stroke*. 2023;54(7):1930–1942.

59. Leibovich SJ, Ross R. The role of the macrophage in wound repair. A study with hydrocortisone and antimacrophage serum. *Am J Pathol*. 1975;78(1):71–100.

60. Vallelian F, et al. Revisiting the putative role of heme as a trigger of inflammation. *Pharmacol Res Perspect*. 2018;6(2):e00392.

61. Korolnek T, Hamza I. Macrophages and iron trafficking at the birth and death of red cells. *Blood*. 2015;125(19):2893–2897.

62. Boyle JJ, et al. Activating transcription factor 1 directs Mhem atheroprotective macrophages through coordinated iron handling and foam cell protection. *Circ Res*. 2012;110(1):20–33.

63. Pfefferlé M, et al. Acute Hemolysis and Heme Suppress Anti-CD40 Antibody-Induced Necro-Inflammatory Liver Disease. *Front Immunol*. 2021;12:680855.

64. Vallelian F, et al. Heme-stress activated NRF2 skews fate trajectories of bone marrow cells from dendritic cells towards red pulp-like macrophages in hemolytic anemia. *Cell Death Differ*. 2022;29(8):1450–1465.

65. Pfefferlé M, et al. Antibody-induced erythrophagocyte reprogramming of Kupffer cells prevents anti-CD40 cancer immunotherapy-associated liver toxicity. *J Immunother Cancer*. 2023;11(1):e005718.

66. Consonni FM, et al. Heme catabolism by tumor-associated macrophages controls metastasis formation. *Nat Immunol*. 2021;22(5):595–606.

67. Kim SH, et al. Breast cancer cell debris diminishes therapeutic efficacy through heme oxygenase-1-mediated inactivation of M1-like tumor-associated macrophages. *Neoplasia*. 2020;22(11):606–616.

68. Alaluf E, et al. Heme oxygenase-1 orchestrates the immunosuppressive program of tumor-associated macrophages. *JCI Insight*. 2020;5(11):e133929.

69. Osuka S, Van Meir EG. Overcoming therapeutic resistance in glioblastoma: the way forward. *J Clin Invest*. 2017;127(2):415–426.

70. Sharma P, et al. Primary, Adaptive, and Acquired Resistance to Cancer Immunotherapy. *Cell*. 2017;168(4):707–723.

71. Taguchi K, et al. Genetic analysis of cytoprotective functions supported by graded expression of Keap1. *Mol Cell Biol*. 2010;30(12):3016–3026.

72. Kong X, et al. Enhancing Nrf2 pathway by disruption of Keap1 in myeloid leukocytes protects against sepsis. *Am J Respir Crit Care Med*. 2011;184(8):928–938.

73. Reddy NM, et al. Conditional deletion of Nrf2 in airway epithelium exacerbates acute lung injury and impairs the resolution of inflammation. *Am J Respir Cell Mol Biol*. 2011;45(6):1161–1168.

74. Bankhead P, et al. QuPath: Open source software for digital pathology image analysis. *Sci Rep*. 2017;7(1):16878.

75. Wolf FA, Angerer P, Theis FJ. SCANPY: large-scale single-cell gene expression data analysis. *Genome Biol*. 2018;19(1):15.

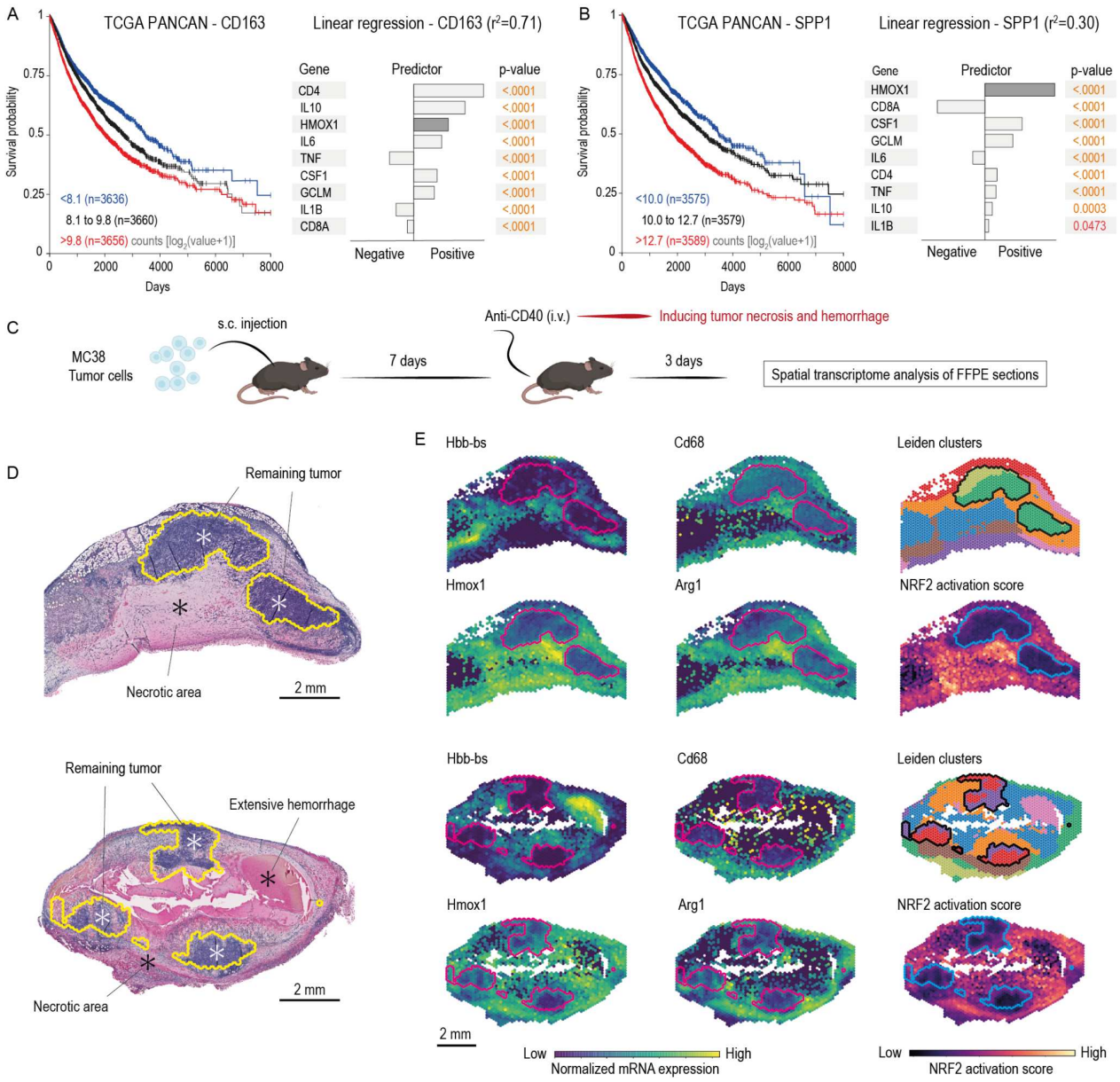

Figure 1. RBC and heme-exposure defines an identity of tumor-associated macrophages

A Kaplan–Meier survival analysis stratified by *CD163* mRNA expression in patients with solid cancers in the TCGA PANCAN database (left); linear regression model with *CD163* as the response variable and tissue microenvironmental factors as the predictors (r^2=0.71).

B. Kaplan–Meier survival analysis stratified by *SPP1* mRNA expression in patients with solid cancers in the TCGA PANCAN database (left); linear regression model with *SPP1* as the response variable and the tissue microenvironmental factors as predictors (r^2=0.30).

C. MC38 tumor-bearing mice were treated with agonistic anti-CD40 antibodies to induce hemorrhagic tumor necrosis. Spatial RNA-seq analysis was performed to characterize macrophages in the perinecrotic tumor microenvironment.

D. H&E-stained MC38 tumor sections used for transcriptional analysis. Bar scale = 2 mm. Marked areas indicate the remaining tumoral tissue.

E. Expression of selected genes, highlighting the presence of *Cd68*$^{+}$*Hmox1*$^{+}$*Arg1*$^{+}$ macrophages in the hemorrhagic (Hb-bs^{+}) tumor regions. The *Cd68*$^{+}$*Hmox1*$^{+}$*Arg1*$^{+}$ regions are marked by a high NRF2 activation score. The lines delineate the remaining tumor.

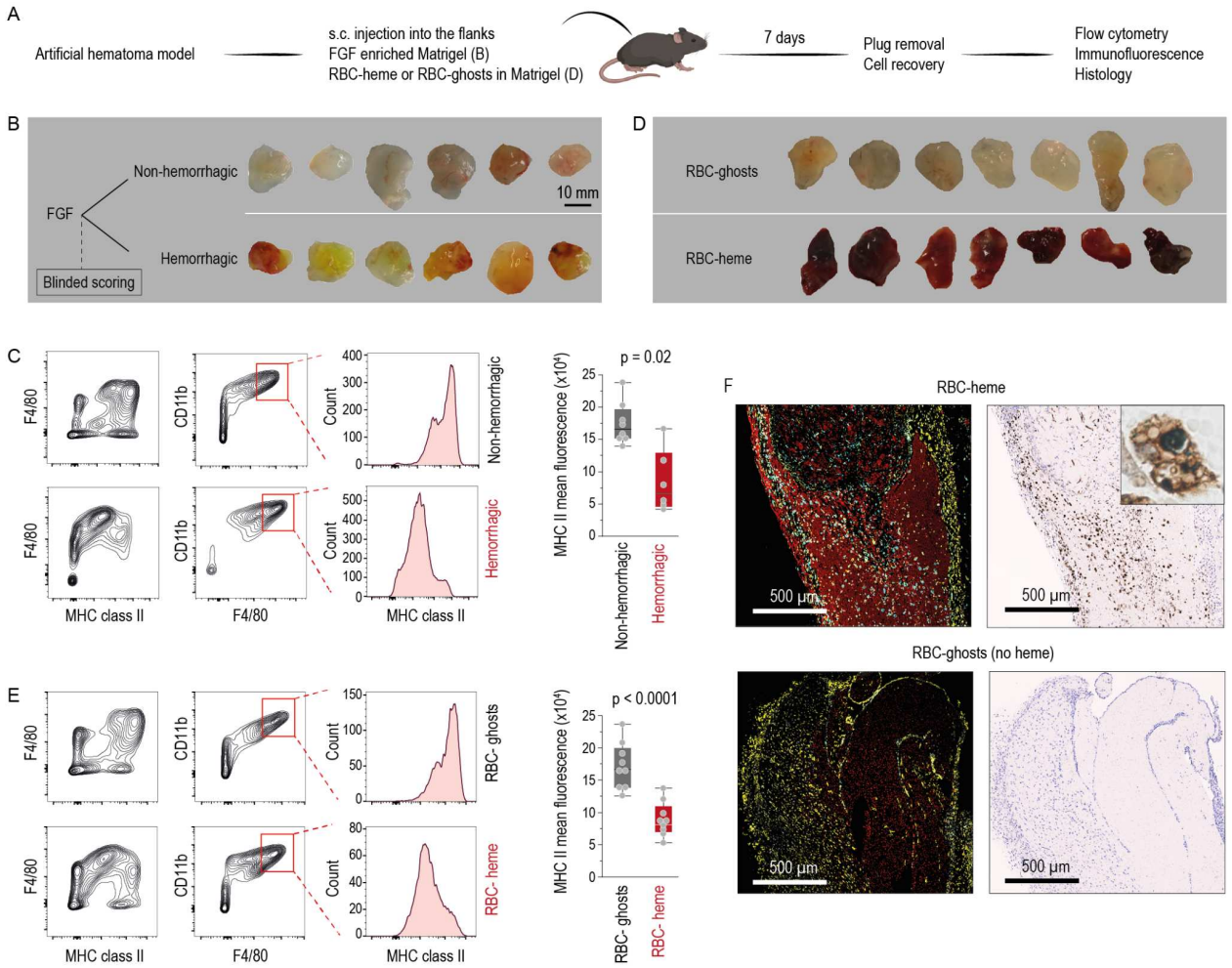

Figure 2. Erythrophagocytic transformation of macrophages in RBC-heme Matrigel plugs

A. Subcutaneously placed FGF-enriched Matrigel plugs were used to study the effect of hemorrhage on the phenotype of invading macrophages. Plugs enriched with intact RBCs (RBC-heme) or RBC-ghosts were used to study the specific effect of hemoglobin-heme.

B. FGF-enriched Matrigel plugs were collected from the subcutaneous (s.c.) injection site seven days after injection and classified by blinded investigators as non-hemorrhagic or hemorrhagic based on their macroscopic appearance.

C. Flow cytometry contour plots of plug-invading cells, defining F4/80$^+$ CD11b$^+$ macrophages with lower MHC class II expression in hemorrhagic plugs. The box plots depict the mean fluorescence intensities of MHC class II expression within the CD11b$^+$ F4/80$^+$ population (n= 6-8 plugs per condition, each dot represents one plug; t-test).

D. RBC-heme and RBC-ghost plugs were collected seven days after s.c. injection.

E. Flow cytometry contour plots of plug-invading cells defining F4/80$^+$CD11b$^+$ macrophages with lower MHC class II expression in RBC-heme than RBC-ghost plugs. The box plots depict the mean fluorescence intensities of MHC class II expression within the CD11b$^+$F4/80$^+$ population (n= 9 plugs per condition, each dot represents one plug; t-test).

F. Fluorescence immunohistochemistry images of Matrigel plug sections stained with TER119 (red, RBC-heme or RBC-ghost), anti-F4/80 (yellow, macrophages), and anti-HMOX1 antibodies (cyan). Nuclei were stained with DAPI (white). Images were acquired using a Phenolmager HT (Akoya). Corresponding consecutive sections stained for iron show iron accumulation in infiltrating cells. Scale bar = 500 µm. The insert shows an iron-positive erythrophagocyte containing multiple RBC remnants.

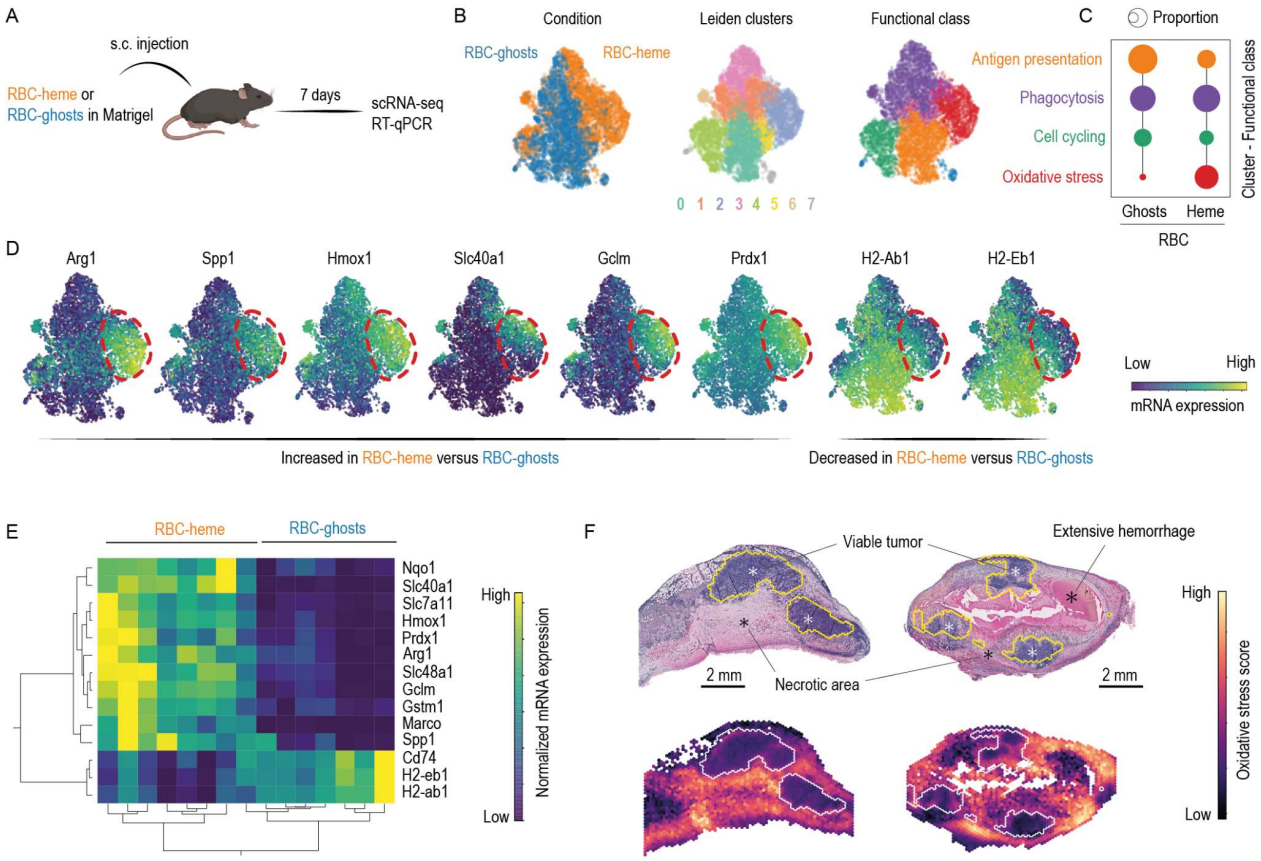

Figure 3. RBC-heme enforces the transformation of macrophages into heme-TAMs

A. RBC-heme and RBC-ghost-enriched Matrigel plugs were collected seven days after s.c. placement and processed for scRNA-seq analysis.

B. Plug-invading cells were enriched by anti-F4/80 and anti-CD11b magnetic beads from an RBC-heme and an RBC-ghost Matrigel plug before scRNA-seq analysis. UMAPs are color-coded for condition, Leiden cluster, and the attributed functional class.

C. Proportion of macrophages per functional class stratified for RBC-heme and RBC-ghost. The dot size corresponds to the proportion of cells (%) per functional class. This analysis visualizes that erythrophagocytosis fosters the emergence of oxidative stress-handling macrophages while suppressing cells equipped for antigen presentation.

D. Expression heatmaps of selected signature genes. The dashed line highlights the region of the UMAP containing the oxidative stress cluster. These macrophages have high expression of *Arg1*, *Spp1*, heme-, iron-, and oxidative stress-handling genes, while expression of MHC class II-related genes is low.

E. Expression heatmap and unsupervised hierarchical clustering analysis of heme-TAM marker genes measured by RT–qPCR in plug-invading cells after enrichment of F4/80$^+$ cells. Each column represents data from one plug collected seven days after s.c. injection (n = 8 RBC-heme plugs, n=7 RBC-ghost plugs).

F. A score for the oxidative stress-related macrophages in the RBC plug was calculated based on

differentially expressed genes (log2FC > 2, *p-value* < 0.001, n = 114 genes). This score was mapped into the spatial transcriptome data of the MC38 tumor sections reported in Figure 1. The heatmap visualizes that macrophages with an oxidative stress-handling identity accumulate in the perinecrotic tumor microenvironment.

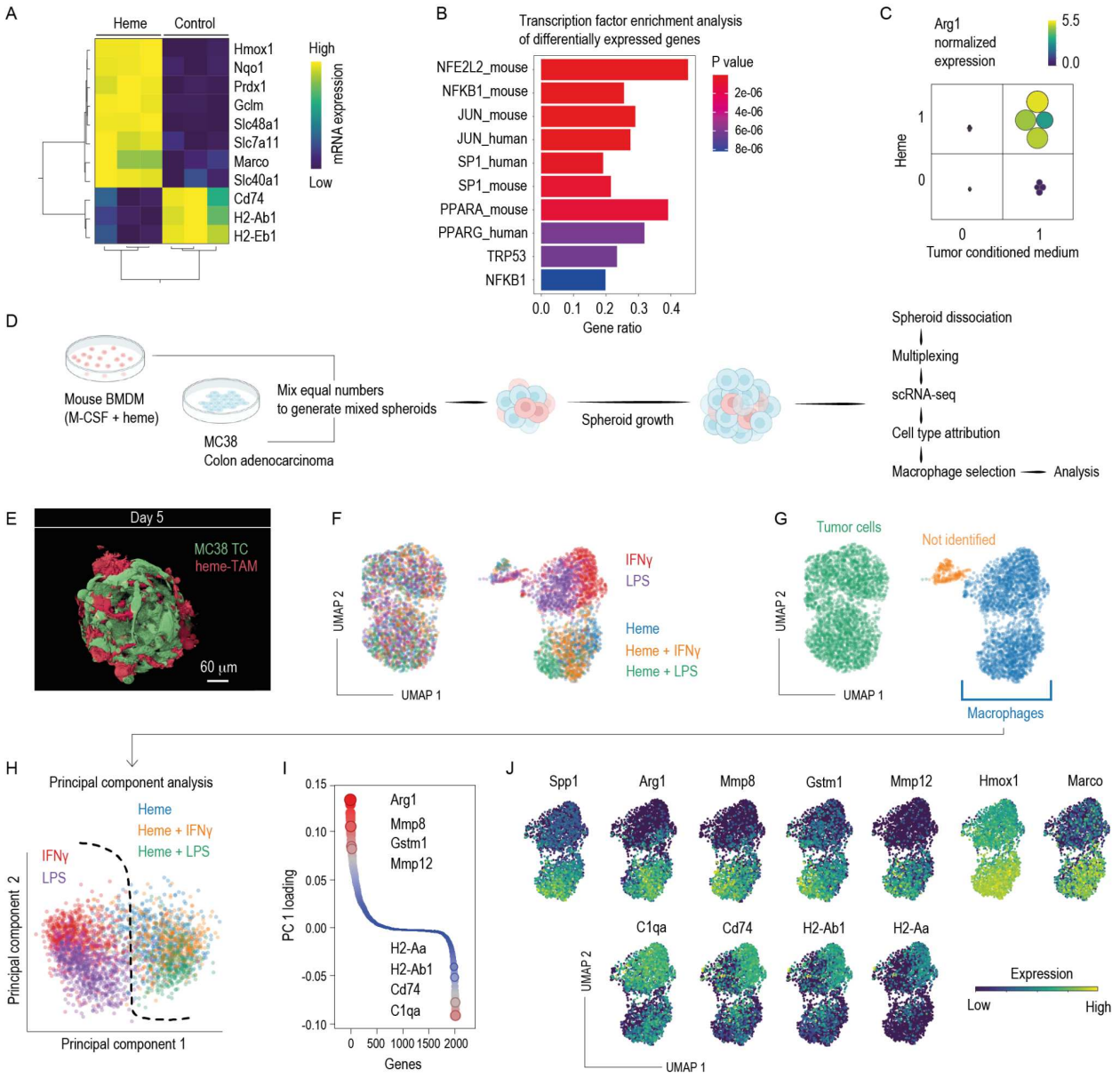

Figure 4. Heme-TAMs in 3D spheroid cancer cell cultures

A. Expression heatmap and unsupervised hierarchical clustering analysis of marker genes quantified by bulk RNA-seq in control and heme-treated BMDMs cultured in 2D (normalized log2 counts). Each column represents macrophages from one mouse (n=3).

B. EnrichR analysis of all significantly differentially expressed genes (log2FC > 0.5, *p-value* < 0.001, n=3). The gene ratio defines the overlap of the input genes and the term-associated genes, and the top 10 enriched terms are shown. Terms are ranked by their p-value.

C. Results of a factorial experiment defining the synergistic effect of heme and MC38 cell culture supernatant on *Arg1* mRNA expression in 2D BMDM cultures. *Arg1* expression was measured by RT–qPCR. The color and size of the dots represent the normalized gene expression per sample (n = 4 BMDM cultures per condition).

D. Experimental workflow used to generate and analyze mixed cell-type 3D-spheroids containing MC38 tumor cells and BMDMs.

E. 3D reconstruction of a confocal microscopy image stack of a mixed cell-type spheroid resulting from a 5-day culture of GFP-MC38 cells (green) and heme-TAM-tomato cells (red) in a microwell plate. Scale bar = 60 μm.
F. Results of a multiplexed scRNA-seq experiment with mixed cell-type spheroids containing MC38 cells and BMDMs that have been pretreated with heme, LPS, IFNγ, or combinations thereof. The spheroids were collected for scRNA-seq 24 hours after the two cell types were mixed and seeded on microwell plates. The UMAP is color-coded to indicate the BMDM pretreatment.
G. Cell-type assignment of the spheroid cells was performed, and macrophages were extracted for further analysis.
H. In the PCA of spheroid macrophages, PC1 segregates the heme-pretreated BMDMs from those not pretreated with heme.
I. The contribution of individual genes to PC1 is expressed as loadings. Genes are ordered and color-coded by their PC1 loading. A high absolute value indicates that the gene strongly influences overall gene expression variance. The highest PC1 loading was found for *Arg1*.
J. Expression heatmaps of the top PCA drivers and selected heme-induced TAM marker genes.

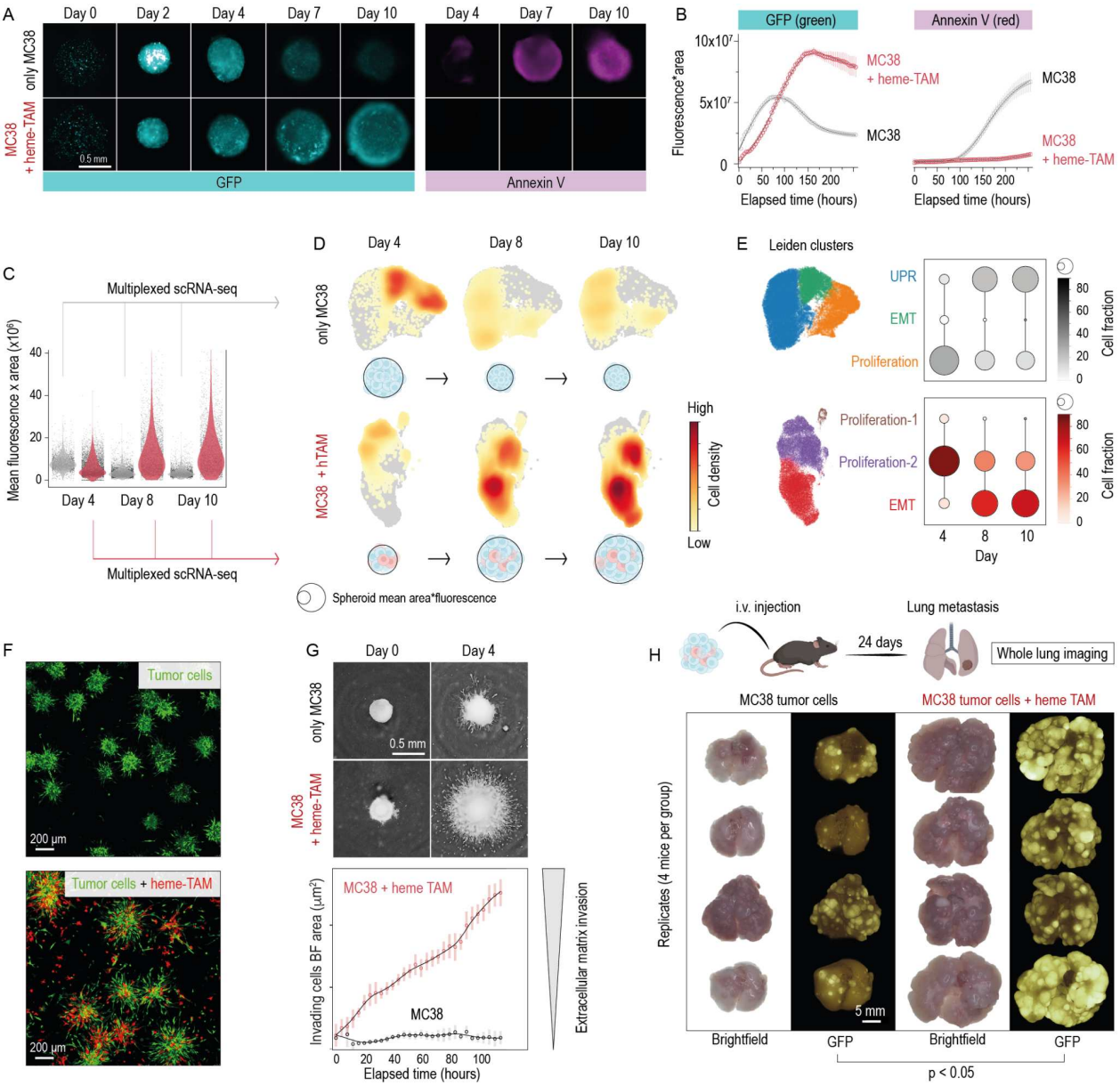

Figure 5. Heme-TAMs support tumor cell growth, invasiveness, and metastasis

A. 3D spheroids of only GFP-MC38 cells or GFP-MC38 cells mixed with heme-TAMs grown in ultralow adherence plates. GFP fluorescence (magenta) and annexin V (cyan) were imaged with a live cell imaging system for 10 days. Representative images for each condition are shown.

B. Integrated GFP and annexin V fluorescence intensities across the spheroid area over time, demonstrating enhanced spheroid growth and no apoptosis in the presence of heme-TAMs. Data are the mean ± 95% CI of 42 replicates analyzed within one representative experiment.

C. Spheroids were grown in microwell plates for scRNA-seq experiments. Immediately before processing, the spheroids were scanned with a fluorescence microscope. Integrated GFP fluorescence across the spheroid area was quantified for > 3000 spheroids per condition and used for cell density correction in (F) (gray = MC38, red = MC38 + heme-TAMs) (each dot represents one spheroid, ANOVA with Tukey–Kramer posttest corrected with p-value < 0.001 for all comparisons, except MC38 day 8 vs. MC38 day 10, p-value = 0.99).

D. Two scRNA-seq experiments were performed to define the transcriptional state of MC38 tumor cell spheroids (only MC38) or mixed cell-type spheroids (MC38 + heme-TAM) at different time points. Each was a multiplexed experiment with spheroids collected on days 4, 8, and 10 post-formation. After macrophage exclusion, cell densities were scaled by the mean spheroid size per condition before projecting on the UMAP.
E. Leiden clustering defined 3 clusters per experiment, and a dominant functional annotation for each cluster was determined by GSEA using the hallmark gene sets of the Molecular Signature Database (MSigDB). The dot plots depict the fraction of tumor cells within each functional state per time point (UPR: unfolded protein response; EMT: epithelial-mesenchymal transition). The data demonstrate that in the absence of heme-TAMs, MC38 progress towards UPR. In the presence of heme-TAMs, the tumor cells reach a stable EMT state.
F. GFP-MC38 spheroids (top) and mixed GFP-MC38 + heme-TAM-tomato spheroids (bottom) were transferred from microwell plates to a flat glass-bottom plate on day 4 after spheroid formation and embedded into an extracellular matrix. Cell invasion into the matrix was imaged qualitatively with a confocal microscope 24 hours later.
G. Quantitative spheroid invasion assay. Four days post-formation, spheroids were embedded into an extracellular matrix (t = 0h), and cell invasion was measured with a live cell imaging system every 4 hours. Top: representative inverted bright field images. Scale bar = 0.5 mm. Bottom: the invading cell front was automatically segmented and quantified over time. Data are the mean ± 95% CI of 21 replicates analyzed within one representative experiment.
H. Approximately 750 spheroids per condition were collected from microwell plates on day 5 post-formation and injected intravenously (i.v.) into C57BL/6J mice. Lungs were collected 24 days after injection. Brightfield and GFP fluorescence whole lung images were used to visualize and quantify metastasis formation, which was exacerbated when the injected GFP-MC38 spheroids contained heme-TAMs. t-test. Scale bar = 5 mm.

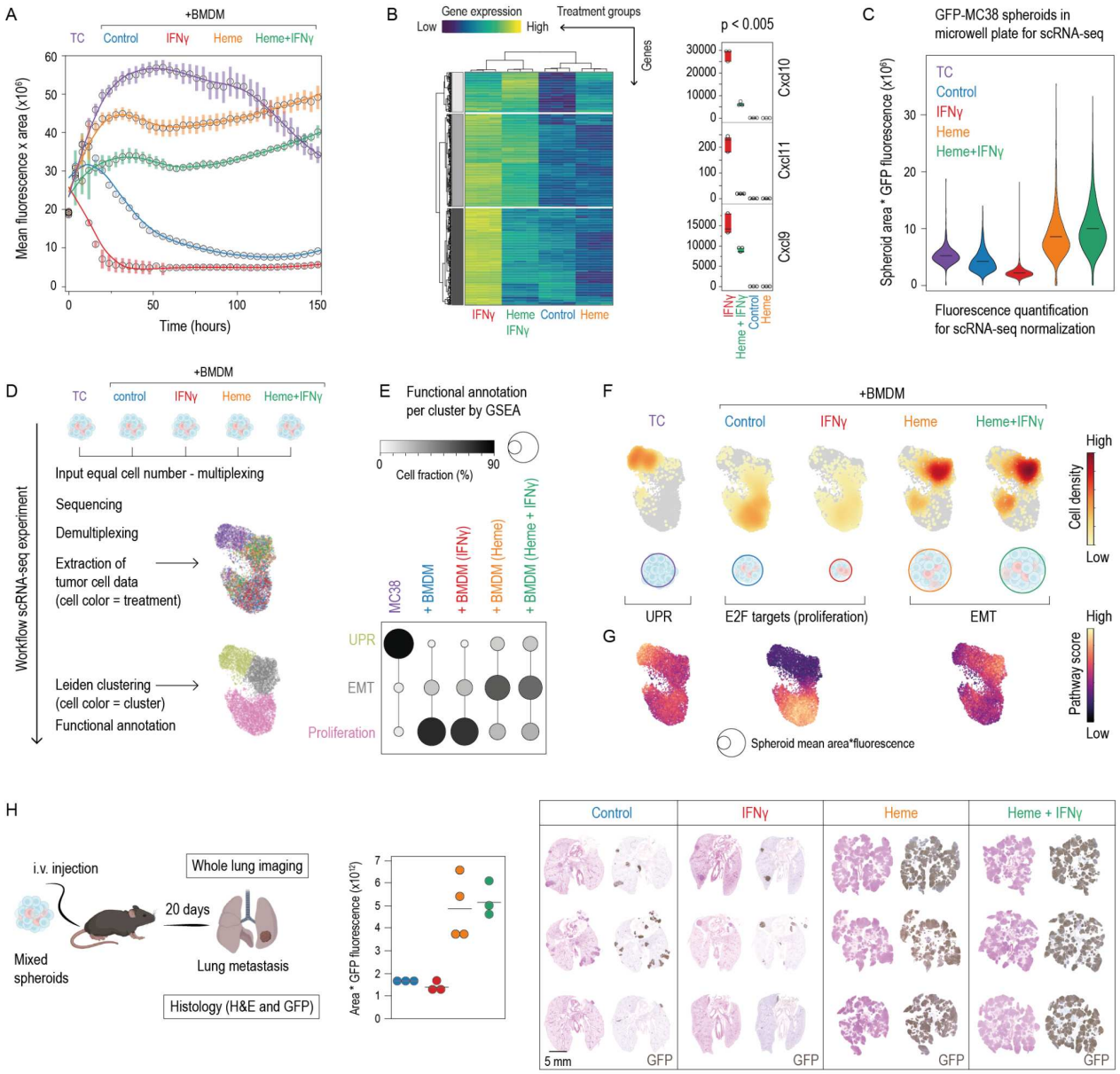

Figure 6. Heme-TAMs resist tumoricidal transformation by IFNγ

A. Live cell microscopy of GFP-MC38 tumor cell spheroids (TC) and mixed spheroids of GFP-MC38 cells with BMDMs that were untreated (control) or pretreated with IFNγ, heme, or heme+IFNγ. Data represent the GFP fluorescence intensity integrated across the object area. Data are the mean ± 95% CI of 10 replicates analyzed within one representative experiment.

B. Expression heatmap and hierarchical clustering of differentially expressed genes in IFNγ-treated versus control BMDMs, with and without heme pretreatment (log2FC > 0.5, *p-value* < 0.005, n=3). The data reveal that heme suppresses IFNγ-induced gene expression. Plots on the right: Normalized count data for *Cxcl9*, *Cxcl10*, and *Cxcl11*. Each point represents one biological replicate.

C. Spheroids identical to those in (A) were grown in microwell plates for downstream analysis by scRNA-seq. On day 9 after spheroid formation, the whole plate was scanned with a fluorescence microscope before spheroids were further processed. Violin plots depict the GFP fluorescence

intensity integrated across the object area for > 1400 spheroids per condition (ANOVA with Tukey–Kramer posttest corrected with p< 0.001 for each comparison). The plots highlight the IFNγ-enhanced tumoricidal activity of macrophages, which is abandoned by heme pretreatment.
D. Workflow of a multiplexed scRNA-seq experiment analyzing the spheroids described in (C). Tumor cell data were extracted from the whole dataset for downstream analysis before three Leiden clusters were defined, which were then functionally annotated by GSEA.
E. GSEA-defined dominant functional attributes for the three tumor cell clusters. The dot plot visualizes the fraction of tumor cells within each functional state per condition. Confirming that heme-pretreated BMDMs support EMT of tumor cells irrespective of concurrent IFNγ treatment.
F. Tumor cell densities were normalized by the mean integrated fluorescence of the input spheroids and plotted into the overall UMAP of the multiplexed experiment. This visualizes the macrophage-dependent differential tumor cell states. The bubble beneath the UMAP depicts the mean spheroid size per condition.
G. Gene expression score intensities for the three functional GSEA categories.
H. Approximately 750 spheroids (GFP-MC38 cancer cells + BMDMs) were collected from microwell plates on day 4 after spheroid formation and injected i.v. into *Rag2*$^{-/-}$*γc*$^{-/-}$ mice to study their metastatic potential. Lungs were collected 20 days after injection. Paraffin sections of lung tissue (H&E and GFP stainings) were used to visualize the extent of metastatic disease. Scale bar = 5 mm. The GFP fluorescence based on whole-lung fluorescence imaging (see Supplementary Figure 4E) was integrated across the imaged lung area and quantified for n=3-4 animals per condition. Each dot represents one mouse (lung). ANOVA with Tukey–Kramer posttest corrected for multiple comparisons, IFNγ vs. heme + IFNγ p 0.0028, heme + IFNγ vs. control p 0.0046, heme vs. IFNγ p 0.0030, heme vs. control p 0.0051, control vs. IFNγ p 0.98, heme vs. heme + IFNγ p 0.97.

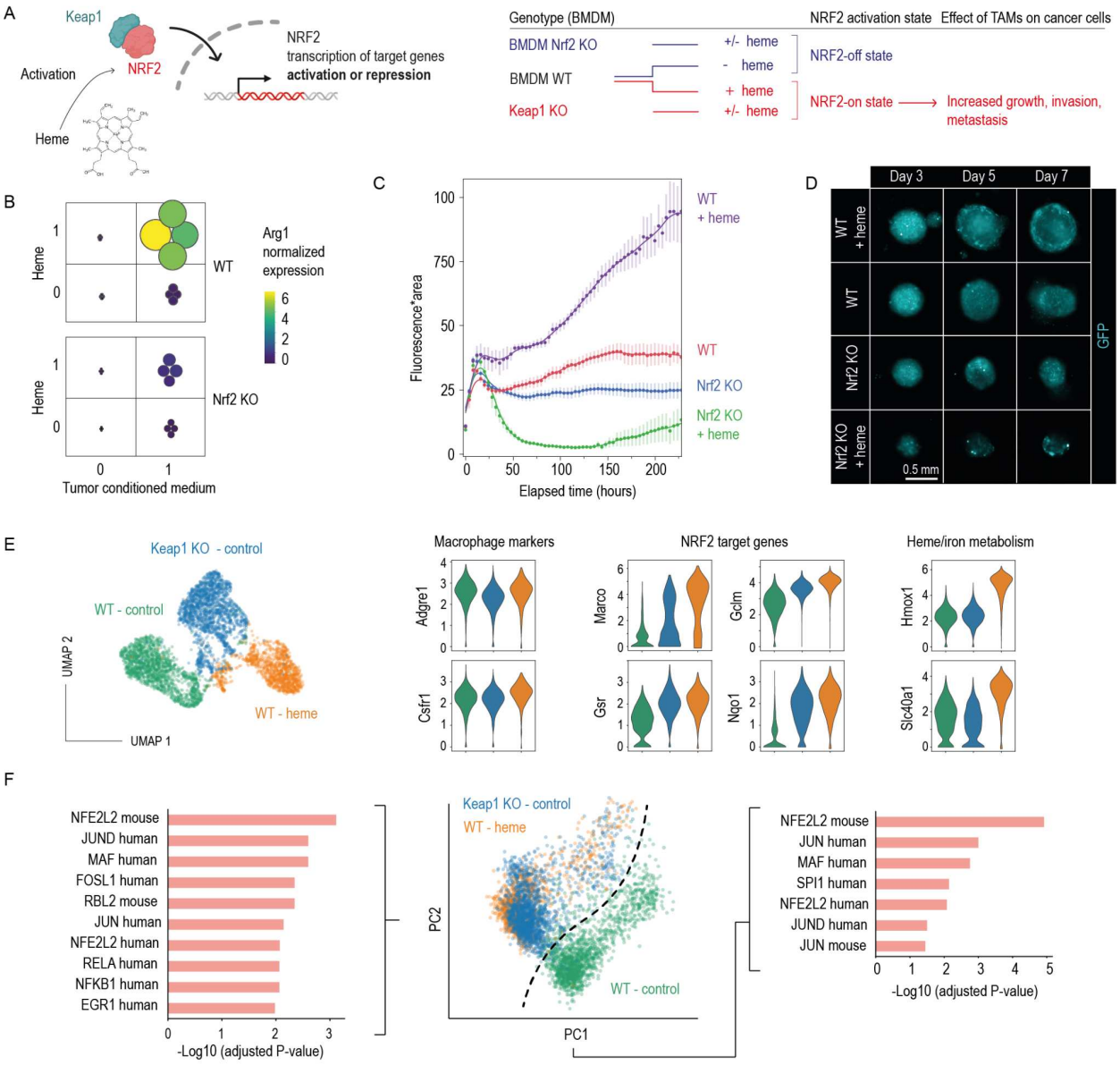

Figure 7. Heme-TAM transformation progresses via NRF2 signaling

A. *Keap1* and *Nrf2* knockout (KO) mice generated BMDMs with locked NRF2-on and NRF2-off states, independent of heme exposure.

B. Factorial experiment defining the effect of heme treatment and MC38 cell culture supernatant on the expression of *Arg1* mRNA measured by RT–qPCR in *Nrf2* WT and *Nrf2* KO BMDMs. The color and size of the dots indicate the normalized gene expression per sample (n=4 per condition). The data demonstrates that NRF2 is required to leverage the synergistic effect of heme and tumor cell supernatant.

C. Live cell microscopy analysis of spheroids of GFP-MC38 cancer cells mixed with *Nrf2* KO and *Nrf2* WT BMDMs that were untreated or pretreated with heme. Data represent the GFP fluorescence intensity integrated across the object area. Data are the mean ± 95% CI of 15 replicates analyzed within one representative experiment.

D. Representative fluorescence images of spheroids. Scale bar = 0.5mm.

E. Multiplexed scRNA-seq experiment of untreated 2D cultured WT BMDMs, heme-treated WT BMDMs, and untreated *Keap1* KO BMDMs. The UMAP visualizes that the interaction of genotype and treatment defines distinct gene expression patterns. The violin plots visualize the expression of canonical myeloid marker genes, NRF2-regulated genes, and heme metabolism genes as log10 (norm. count + 1) values.
F. PCA of the transcriptome data described in (E). The genes defining PC1 and PC2 were analyzed for driver transcription factors by EnrichR using the TRRUST Transcription Factors 2019 dataset. This analysis indicates that heme-treated BMDMs and *Keap1* KO macrophages share activated NRF2 as a driver of their phenotype.

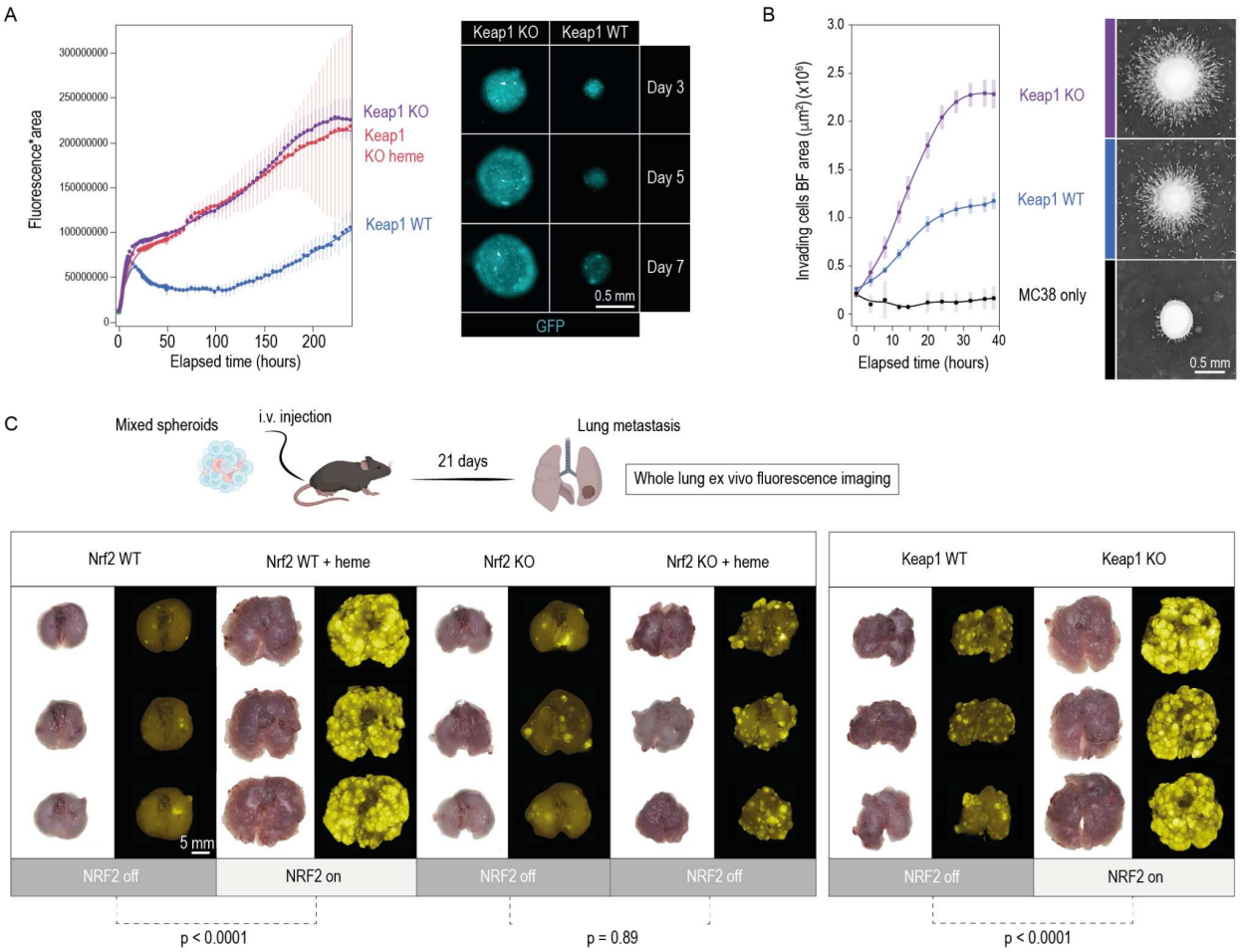

Figure 8. Active NRF2 in TAMs enhances tumor invasiveness and metastatic disease

A. Live cell microscopy analysis of spheroids of GFP-MC38 cancer cells mixed with untreated WT BMDMs and untreated as well as heme-pretreated *Keap1* KO BMDMs. Data represent the GFP fluorescence intensity integrated across the object area and demonstrate that *Keap1* KO in macrophages mimics the procancerous effect of heme. Data are the mean ± 95% CI of 25 replicates analyzed within one representative experiment. GFP fluorescence images of mixed spheroids containing untreated *Keap1* WT BMDMs and untreated *Keap1* KO BMDMs on days 3, 5, and 7 after spheroid formation.

B. Quantitative spheroid invasion assay. Four days post-formation, spheroids were embedded into an extracellular matrix (t = 0h), and cell invasion was measured with a live cell imaging system. The invading cell front was automatically segmented and quantified over time. Data are the mean ± 95% CI of 20 replicates analyzed within one representative experiment. Representative bright field images of spheroids 16 hours after matrix embedding are shown on the right; scale bar = 0.5 mm. For better visualization, the images were inverted.

C. To test the metastatic potential, approximately 750 spheroids per condition were collected from microwell plates at day 4 post-spheroid formation and injected i.v. into *Rag2*$^{-/-}\gamma c^{-/-}$ mice. Lungs were collected 21 days after injection. Brightfield and GFP fluorescence whole lung images were used to visualize metastases, which were extensive when NRF2 was active in macrophages. Scale bar = 5 mm. Whole-lung GFP fluorescence intensity was integrated across the lung image area. ANOVA with Tukey–Kramer posttest corrected for multiple comparisons.

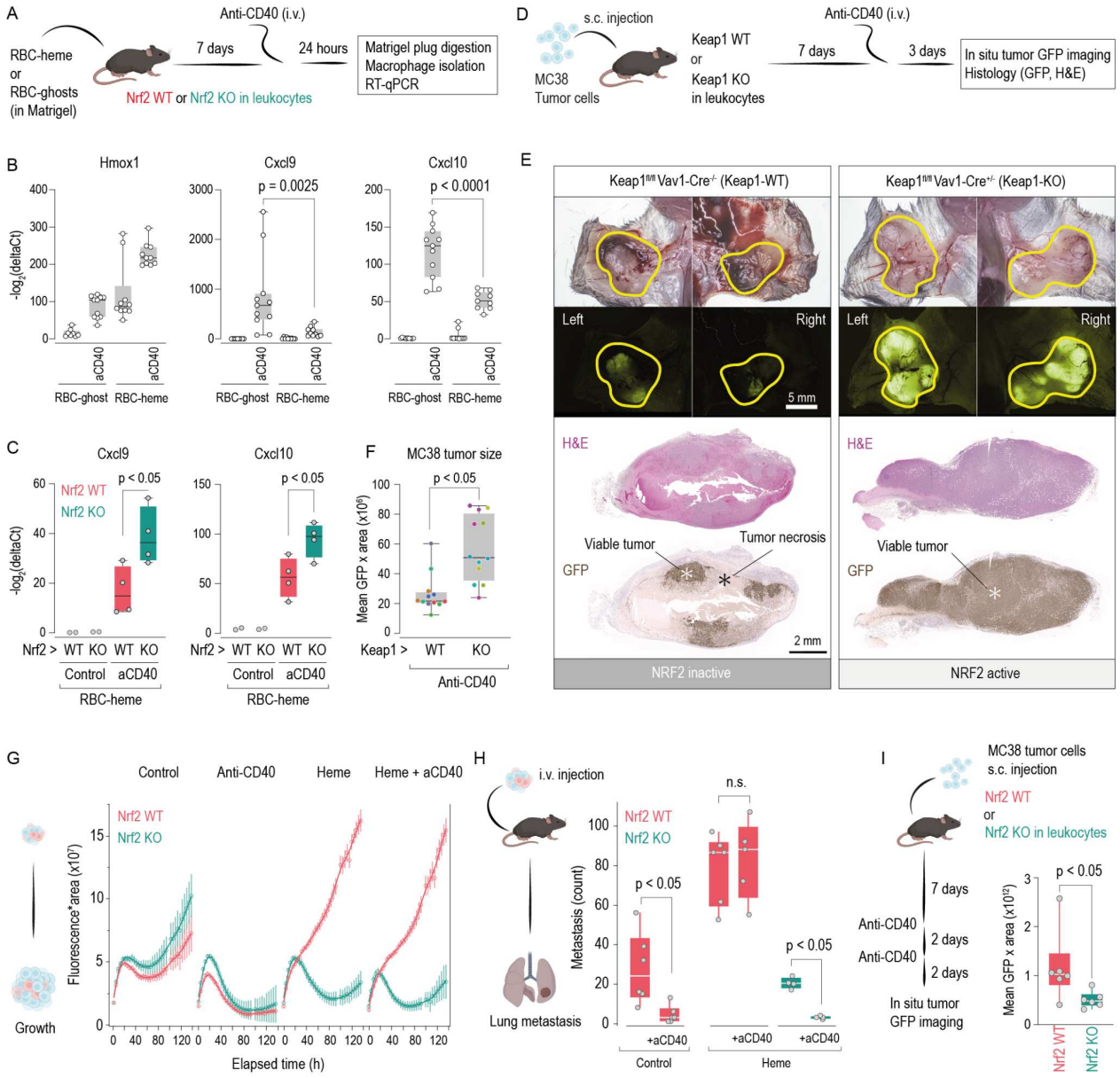

Figure 9. NRF2 signaling in hematopoietic cells promotes resistance to immunotherapy

A. Matrigel plugs enriched with RBC-heme or RBC-ghost were s.c. placed in mice. On day 7, the mice were treated with anti-CD40 antibodies to activate macrophages, and the plugs were explanted 24 hours later. Macrophages were enriched from the digested plugs using F4/80 magnetic beads, and gene expression was measured by RT-qPCR.

B. Relative mRNA expression of *Hmox1*, *Cxcl9*, and *Cxcl10* in macrophages. Each dot represents one plug (n=8-11), ANOVA with Tukey–Kramer posttest corrected for multiple comparisons.

C. To define the role of NRF2 in the RBC-heme-suppressed cytokine response, identical experiments were performed with RBC-heme plugs placed in conditional *Nrf2* WT and KO mice, yielding a more pronounced anti-CD40-induced response in the *Nrf2* KO mice.

D. MC38 tumor cells were s.c. injected into conditional *Keap1* WT or KO mice. On day 7, the mice were treated with anti-CD40 antibodies. The tumors were collected for analysis three days later.

E. Top: Representative brightfield and GFP fluorescence images visualizing MC38 tumors in situ.

Scale bar = 5 mm. Bottom: Representative sections of tumors stained with H&E and anti-GFP. Scale bar = 2 mm.

F. GFP fluorescence intensity was integrated across the tumor image area. Each dot represents one tumor grown on the right and left flank of a mouse, and the dot color indicates the mouse of origin (n=12), Wilcoxon test.

G. Live cell microscopy analysis of spheroids of GFP-MC38 cancer cells mixed with *Nrf2* KO and *Nrf2* WT BMDMs that were untreated or pretreated with heme ± crosslinked anti-CD40 antibody. Data represent the GFP fluorescence intensity integrated across the object area. Data are the mean ± 95% CI of 15 replicates analyzed within one representative experiment.

H. To study how macrophage activation by anti-CD40 antibodies changes the metastatic potential of spheroids, we collected spheroids on day 4 post-formation and injected approximately 750 spheroids i.v. per mouse. Lungs were collected 23 days after injection. Metastatic foci were manually counted on GFP fluorescence whole lung images.
Each dot represents the number of metastatic lesions in one mouse (n=4-6). Wilcoxon test was used to test for the anti-CD40 antibody effect in the three experiments.

I. MC38 tumor cells were s.c. injected into conditional *Nrf2* WT or KO mice. On day 7, the mice were treated with two sequential doses of anti-CD40 antibodies, and tumors were imaged two days later. Each dot represents one tumor (integrated GFP fluorescence intensity across the tumor area, n=6), Wilcoxon test.